THE BELL SYSTEM TECHNICAL JOURNAL
Vol. 58, No. 9, November 1979
Printed in U.S.A.

Transistor Surface Effects Responsible for Anomalous Third-Order Intermodulation Distortion in Undersea Cable Telephone System

By D. G. DUFF and H. M. OLSON

(Manuscript received June 12, 1979)

Anomalous intermodulation distortion has been observed in the SG submarine cable repeater amplifier. The anomalous distortion was found to be dependent upon the crystal orientation in the SG bipolar transistor. This fact suggested that transistor surface effects might be responsible for the anomalous distortion. To test this hypothesis, computer models of the transistor with surface effects were used to compute the third-order modulation coefficient M_3. Surface effects in the collector-base junction alone were modeled by a junction-controlled MOS *capacitor with fast surface states. The* MOS *capacitor model then was added to a modified Gummel-Poon transistor model to simulate surface effects in the complete transistor. It was found that intermodulation contributed by the surface effects was dominant in the case of ⟨111⟩ orientation, and the behavior of the computed intermodulation was similar to the observed behavior. This paper describes the transistor modeling and the intermodulation computations developed in testing the hypothesis. The principal conclusion confirms that the anomalous distortion from the SG transistor is due to surface effects, in particular, to a high surface-state density.*

I. INTRODUCTION

The deviation from perfect linearity in a repeater amplifier for a high-capacity, long-haul system is very small by normal standards. However, when the signal passes through many repeaters, the effect of nonlinear distortion can accumulate to a significant value. The resulting modulation noise of many signals is similar to white noise and is an important factor in the specification of such system parameters as repeater spacing and power-handling capability. Permissible third-

order harmonic distortion at the output of a repeater, for a milliwatt of fundamental, is typically 10^{-10} to 10^{-13} mW.

Measurements of the third-order intermodulation product for the SG submarine cable amplifier showed unusual behavior as power was increased.[1] The deviation from the expected 3-dB increase in third-order power for a 1-dB increase in the three fundamental powers was largest for the case where the fundamental frequencies were slightly lower than the product frequency, as illustrated in Fig. 1. Distortion measurements on the open loop amplifier produced similar results, so the feedback network was not a cause. When the bias voltage and current were varied separately for each of the signal-carrying bipolar transistors in the amplifier, the collector voltage nonlinearity showed

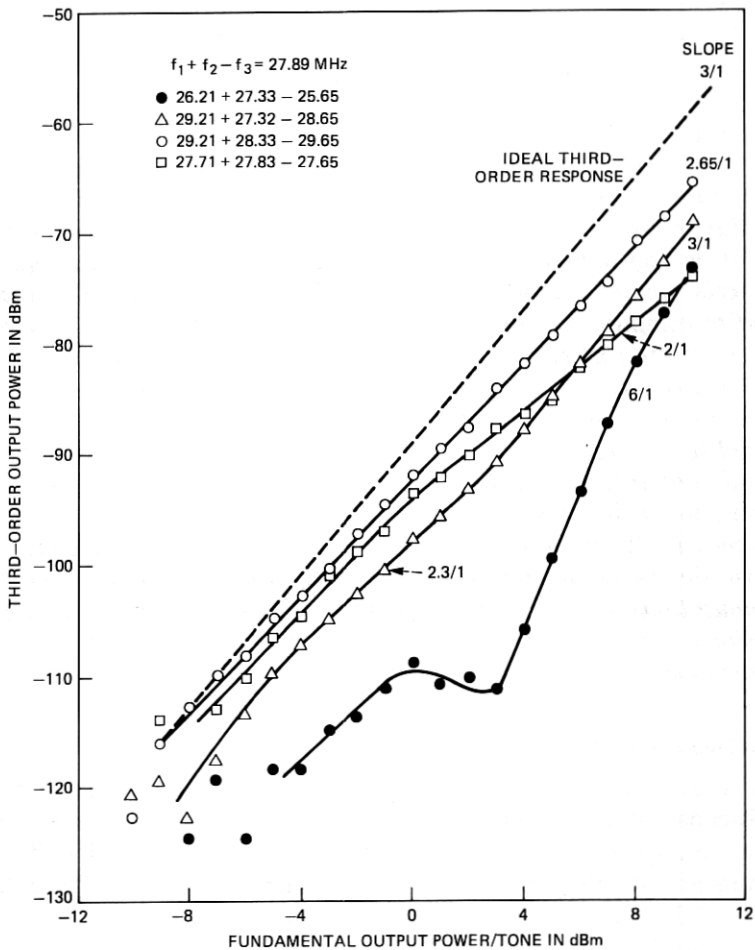

Fig. 1—Distortion in the closed loop SG amplifier.

the most unusual behavior. Two types of silicon transistors with identical geometry but different epitaxial crystal orientations, ⟨111⟩ and ⟨100⟩, were tested in the amplifier. The transistors with ⟨111⟩ orientation showed the unusual distortion characteristics described above, while the transistors with ⟨100⟩ orientation showed classical performance. The distortion performance of the collector-base junction alone showed unusual performance for the ⟨111⟩ orientation and normal performance for the ⟨100⟩ orientation, as shown in Fig. 2.

These measurements suggested that the collector-base junction was the prime source of the unusual distortion. The strong dependence of modulation coefficient M_3 on crystal orientation suggested surface effects as the basic cause of the unusual intermodulation, since surface charge is known to be dependent upon crystal orientation. The SG transistor chip is shown in Fig. 3. The base contact metalization overlaps the collector region with an oxide layer for isolation. This forms a pn junction-controlled MOS capacitor. It is known that the MOS capacitor across the base-collector junction can produce a degradation of transistor distortion.[2] However, the measured junction capacitance for the SG transistors was well-behaved and showed none of the anomalous ripples as a function of voltage, as is expected from large concentrations of surface states. The M_3 measurement of the collector-base junction is a more sensitive test than capacitance measurement and clearly showed anomalous behavior for ⟨111⟩ junctions.

This paper shows that the unusual distortion measured for the collector-base junction of the SG transistor is accurately modeled for both the ⟨111⟩ and ⟨100⟩ crystal orientations by a junction-controlled MOS capacitor with fast surface states. The MOS capacitor model is added to a modified Gummel-Poon transistor model, including the effects of base pushout, lateral spreading, and internal heating to simulate the measured distortion for an SG transistor.

The principal conclusion of this work has been to confirm the hypothesis that the anomalous distortion from the SG submarine cable

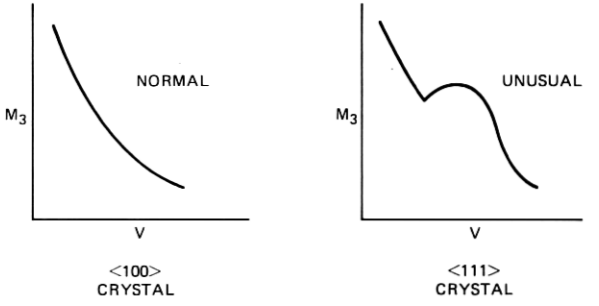

Fig. 2—M_3 vs reverse bias for the collector-base junctions of SG transistors.

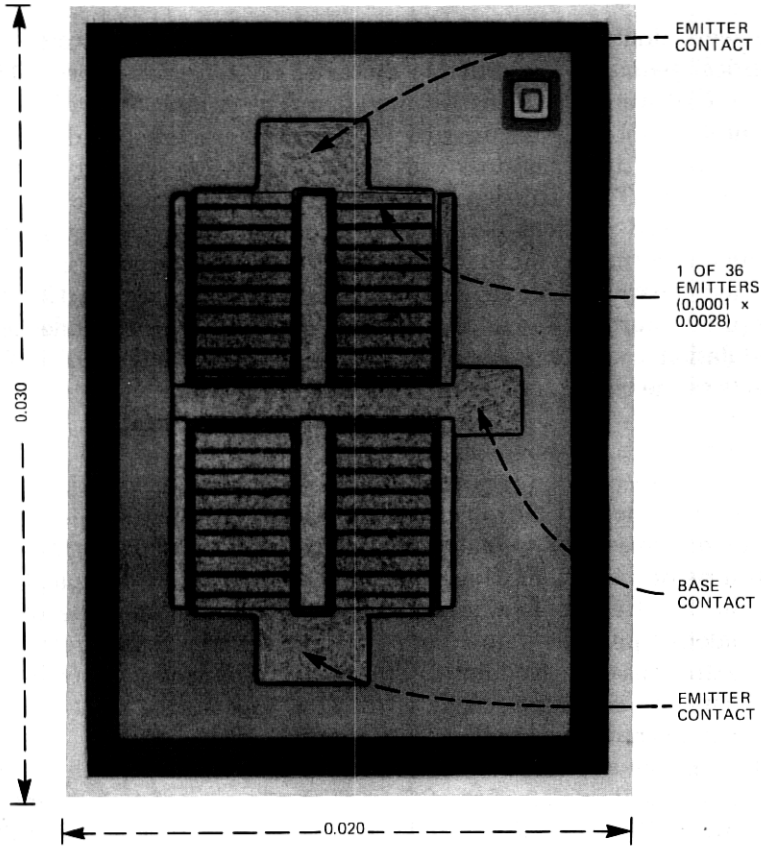

Fig. 3—Transistor chip.

transistor is due to surface effects, in particular to a high surface-state density. Consequently, it is important in designing transistors for applications where intermodulation distortion is critical to take special pains to control and minimize surface effects. This may involve using silicon wafers that are ⟨100⟩ oriented as well as minimizing the collector-base overlap capacitance. Or it may involve special processing steps such as:

(*i*) Routine characterization of transistor surfaces for surface-state and fixed charge densities.

(*ii*) Special annealing or gettering steps to reduce the number of surface states.

Appendix E contains a list of symbols used throughout the paper.

II. DESCRIPTION OF COLLECTOR-BASE JUNCTION MODEL

The transistor is made up of two base regions separated by a base pad, as shown in Fig. 3. Insulated by an SiO_2-SiN layer, the base pad

extends over the collector up to the collector-base junction on each side, as can be seen in Fig. 4. This forms a junction-controlled MOS capacitor with the voltage applied to the junction appearing also across the MOS capacitor, as shown in Fig. 5.[3]

2.1 Nonlinear small-signal ac model

A rather complicated ac circuit model for a junction-controlled MOS capacitor[4] is shown in Fig. 6. C_j represents the junction capacitance between the p-base and n-collector, C_{ox} the oxide capacitance, and C_d the capacitance between the semiconductor-oxide interface and the n-type bulk. C_s models charge storage in the fast interface states at the oxide-semiconductor interface. The resistances characterize the following physical processes:

R_{ns} and R_{ps}—The transition of electrons from the conduction band and holes from the valence band into surface states.

R_{nD} and R_{pD}—The flow of electrons and holes through the surface space-charge layer.

R_{pB}—The generation (or recombination) of holes and their flow rate

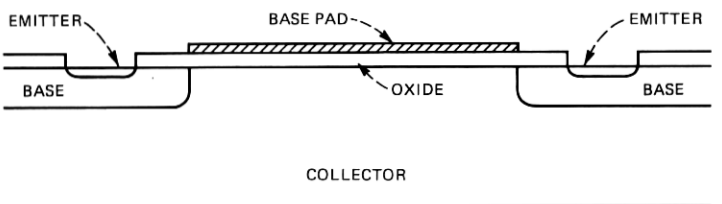

Fig. 4—Cross section of SG transistor.

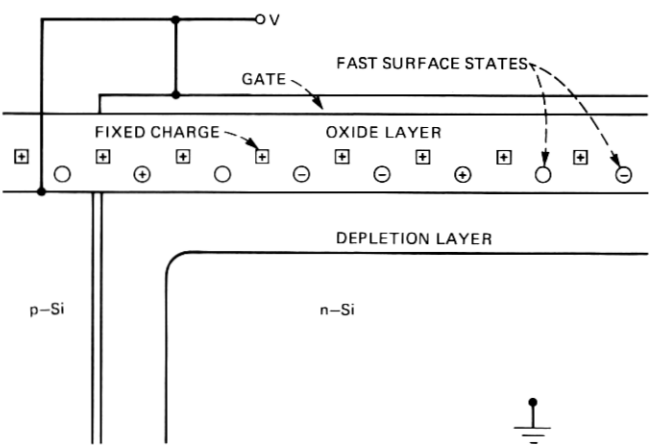

Fig. 5—Schematic of junction-controlled MOS capacitor.

in the region of quasi-neutrality in the bulk adjacent to the space-charge layer.

R_0—The flow of electrons and holes through the bulk of the semiconductor. For an n-type collector, R_I models the average drop in voltage from the base to the semiconductor-oxide interface and helps define the surface quasi-fermi level for holes ψ_{Fp}. The inversion charge is stored in C_I and minority carriers can flow to the surface from the bulk through R_p or through R_I. Holes may be trapped by surface states through R_{ps} and stored in C_s. However, for an n-type collector with positive fixed charge in the oxide, the action of the pn junction on the MOS capacitor is such as to inhibit the semiconductor surface from becoming inverted.

Since electrons are the important carriers for operation in the depletion region, the equivalent circuit shown in Fig. 6 has been

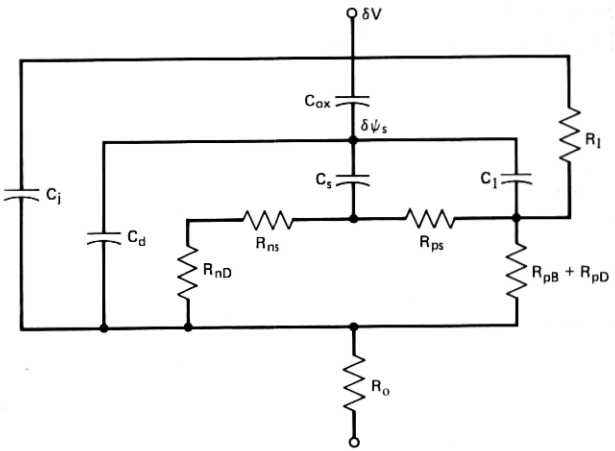

Fig. 6—Alternating-current circuit model for a junction-controlled MOS capacitor on n-type semiconductor.

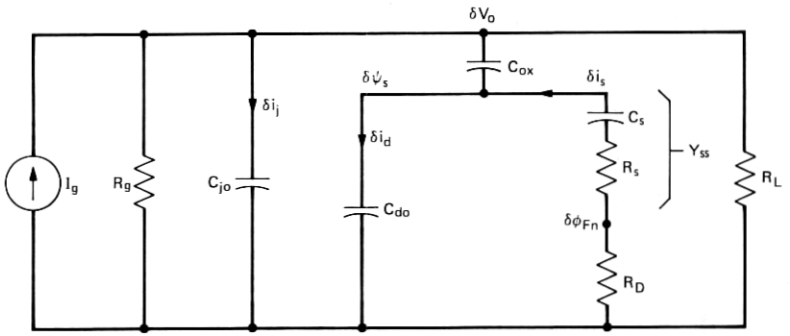

Fig. 7—Simplified ac circuit model of a junction-controlled MOS capacitor.

simplified to that in Fig. 7. Electrons are supplied to the surface from the bulk through R_D which is given by Ref. 4:

$$R_D = \frac{1}{q\mu_n A} \int_0^d \frac{dx}{n_0(x)}, \tag{1}$$

where

μ_n = electron mobility
n_0 = dc electron concentration
d = depletion layer width
A = surface area.

The R_s, C_s network in Fig. 7 is a simple small-signal model for capture and emission of electrons by surface states all located at one energy level within the bandgap. In reality, they are spread throughout the bandgap, and the admittance for a continuum of states of density $N_s(E)$ in the bandgap is given by Ref. 5:

$$Y_{ss} = j\omega \frac{q}{kT} \int_{E_V}^{E_C} \frac{N_s(E) f_0(1 - f_0)}{1 + \dfrac{j\omega f_0}{c_n n_{s0}}} dE, \tag{2}$$

where

$f_0 = [1 + g_s \exp(u - u_F)]^{-1}$ is the fermi function at potential u for a quasi-fermi potential u_F expressed in units of the thermal voltage kT/q
g_s = ground state degeneracy (= 2 for donors, = 1/4 for acceptors)
c_n = electron capture probability
n_{s0} = electron density at the silicon surface established by the bias
E_V, E_C = energy levels at the edges of the valence and conduction bands.

Some authors have argued that the integrand of (2) peaks sharply about the quasi-fermi level with a width of about kT.[6] This would make it easy to integrate (2) if $N_s(E)$ and c_n do not vary much with E over a range of kT. However as is shown in Appendix A, this is the case only at low frequency and high semiconductor doping levels to which these intermodulation computations are not restricted. To preserve accuracy, therefore, integrals of the type exemplified by (2) have been evaluated numerically in this work.

In depletion, the time-constant dispersion measured for MOS capacitors is much broader than that predicted from (2). Good agreement is obtained if one modifies (2) by assuming a statistical fluctuation of surface potential in the plane of the interface.[6] As a first attempt to study intermodulation due to surface states, the surface admittance is

rederived to retain nonlinear terms up to third order for a continuum of surface states. The statistical fluctuation of surface states is taken into account via correction terms derived in Appendix B.

III. COMPUTER ALGORITHMS FOR INTERMODULATION CALCULATIONS

3.1 Volterra series representation

We are interested in computing the third-order modulation coefficient for the circuit of Fig. 7. A convenient way of doing this is by expressing the current through the nonlinear element as a Volterra series of the voltage across the element.[7] If the element is memoryless (purely resistive), the Volterra series simplifies to a power series:

$$i(t) = h_1 v(t) + h_2[v(t)]^2 + h_3[v(t)]^3 + \cdots. \tag{3}$$

If the element has memory (capacitive), the first three terms of the Volterra series are:

$$i_1(t) = \int_0^t h_1(t-\tau)v(\tau)\,d\tau \tag{4}$$

$$i_2(t) = \int_0^t\int_0^t h_2(t-\tau_1, t-\tau_2)\prod_{i=1}^{2} v(\tau_i)\,d\tau_i \tag{5}$$

$$i_3(t) = \int_0^t\int_0^t\int_0^t h_3(t-\tau_1, t-\tau_2, t-\tau_3)\prod_{i=1}^{3} v(\tau_i)\,d\tau_i. \tag{6}$$

The h's in the integrands are known as Volterra kernels of the first, second, and third degree. In the Fourier transform domain, these relations become

$$I_1(\omega) = H_1(\omega)V(\omega) \tag{7}$$

$$I_2(\omega_1, \omega_2) = H_2(\omega_1, \omega_2)\prod_{i=1}^{2} V(\omega_i) \tag{8}$$

$$I_3(\omega_1, \omega_2, \omega_3) = H_3(\omega_1, \omega_2, \omega_3)\prod_{i=1}^{3} V(\omega_i). \tag{9}$$

The transformed Volterra kernels $H_1(\omega)$, $H_2(\omega_1, \omega_2)$, and $H_3(\omega_1, \omega_2, \omega_3)$ may be found from a knowledge of the physics of the device as described in the following sections.

3.2 Volterra kernels for the surface-state admittance in equilibrium (nonlinear case)

The following derivation is strictly valid only for equilibrium conditions, which is a good approximation for an MOS capacitor in deple-

tion with no surface inversion layer. The incremental current flowing from the conduction band for an n-type semiconductor into donor or acceptor surface states within the energy band dE is given by

$$di_s(t) = -\{qN_s(E)c_n[1 - f(t)]n_s(t) - qN_s(E)e_nf(t)\}\, dE, \quad (10)$$

where

$i_s(t)$ = time-varying current flowing into the surface states
q = electron charge
c_n = electron capture probability
$f(t)$ = fermi distribution function
$n_s(t)$ = surface concentration of electrons
e_n = electron emission probability from the surface state.

The incremental current is also equal to the change in charge per unit time

$$di_s(t) = -qN_s(E)\frac{df}{dt}\, dE. \quad (11)$$

Substitute (11) into (10) to get

$$\frac{df}{dt} = c_n(1 - f)n_s - e_nf. \quad (12)$$

This is a nonlinear equation for f in terms of n_s with memory due to the time derivative. Let n_s be the forcing function. Then one desires the small signal components of f about a dc operating point f_0 for small variations in n_s about n_{s0}. So let

$$f = f_0 + \delta f, \quad n_s = n_{s0} + \delta n_s. \quad (13)$$

Substituting (13) into (12) produces a dc equation and an ac equation.

$$e_n = \frac{c_n(1 - f_0)n_{s0}}{f_0} \quad \text{(dc)}. \quad (14)$$

$$\frac{d}{dt}\delta f = c_n(1 - f_0)\delta n_s - \frac{c_nn_{s0}}{f_0}\delta f - c_n\delta f\delta n_s \quad \text{(ac)}. \quad (15)$$

Since the nonlinearity (third term on the right) has memory, a Volterra series may be used to express δf.

$$\delta f = H_1(\omega_a)\ o\ \delta n_s + H_2(\omega_a, \omega_b)\ o\ \delta n_s^2 + H_3(\omega_a, \omega_b, \omega_c)\ o\ \delta n_s^3, \quad (16)$$

where the driving signal δn_s is assumed to consist of three terms:

$$\delta n_s = a_1 \cos(\omega_1 t + \phi_1) + a_2 \cos(\omega_2 t + \phi_2) + a_3 \cos(\omega_3 t + \phi_3) \quad (17)$$

and the circle operator o indicates that the magnitude and phase of

each term in δn_s^n are changed by the magnitude and phase of $H_n(\omega_1, \ldots, \omega_n)$.

The Volterra kernels H_1, H_2, H_3 are derived in Appendix C. The current into the surface states is computed by converting (11) into the frequency domain by using the theorem in Appendix D for differentiating Volterra series and substituting (16) for δf to get

$$di_s(\omega) = -qN_s(E)[j\omega_a H_1(\omega_a) \circ \delta n_s + j(\omega_a + \omega_b)H_2(\omega_a, \omega_b) \circ \delta n_s^2 + j(\omega_a + \omega_b + \omega_c)H_3(\omega_a, \omega_b, \omega_c) \circ \delta n_s^3]\, dE. \quad (18)$$

The total current $i_s(\omega)$ is found by integrating di_s over the band gap, or

$$\begin{aligned} i_s(\omega) = &- j\omega_a q \int_{E_V}^{E_c} N_s(E)H_1(\omega_a)\, dE \circ \delta n_s \\ &- j(\omega_a + \omega_b)q \int_{E_V}^{E_C} N_s(E)H_2(\omega_a, \omega_b)\, dE \circ \delta n_s^2 \\ &- j(\omega_a + \omega_b + \omega_c)q \int_{E_V}^{E_C} N_s(E)H_3(\omega_a, \omega_b, \omega_c)\, dE \circ \delta n_s^3 \\ \equiv\ & G_1(\omega_a) \circ \delta n_s + G_2(\omega_a, \omega_b) \circ \delta n_s^2 + G_3(\omega_a, \omega_b, \omega_c) \circ \delta n_s^3. \end{aligned} \quad (19)$$

In order to use eq. (19), the surface electron concentration δn_s must be known. It may be computed as a nonlinear function of the surface potential ψ_s and the surface quasi-fermi level for electrons ψ_{Fn} to be

$$n_s = n_i \exp[\psi_s - \psi_{Fn})/V_T]. \quad (20)$$

Using a Taylor series expansion

$$\delta n_s = b_1(\delta\psi_s - \delta\psi_{Fn}) + b_2(\delta\psi_s - \delta\psi_{Fn})^2 + b_3(\delta\psi_s - \delta\psi_{Fn})^3, \quad (21)$$

where

$$b_1 = \frac{n_{s0}}{V_T},\ b_2 = \frac{b_1}{2V_T},\ b_3 = \frac{b_2}{3V_T}.$$

Note that the nonlinearity does not have memory, so a Taylor series expansion is sufficient to describe δn_s. Since $i_s = G(n_s)$ and $n_s = B(\psi_s - \psi_{Fn})$, where B and G are functions from (19) and (20), then $i_s = G[B(\psi_s - \psi_{Fn})] \equiv D(\psi_s - \psi_{Fn})$, where the composite function D has a Volterra series as shown below.[7]

$$i_s = D_1(\omega_a) \circ (\delta\psi_s - \delta\psi_{Fn}) + D_2(\omega_a, \omega_b) \circ (\delta\psi_s - \delta\psi_{Fn})^2 + D_3(\omega_a, \omega_b, \omega_c) \circ (\delta\psi_s - \delta\psi_{Fn})^3, \quad (22)$$

where

$$D_1(\omega_a) = G_1(\omega_a) b_1 \tag{23}$$

$$D_2(\omega_a, \omega_b) = G_1(\omega_a + \omega_b) b_2 + G_2(\omega_a, \omega_b) b_1^2 \tag{24}$$

$$D_3(\omega_a, \omega_b, \omega_c) = G_1(\omega_a + \omega_b + \omega_c) b_3 + 2\overline{G_2(\omega_a, \omega_b, + \omega_c)}\, b_1 b_2 + G_3(\omega_a, \omega_b, \omega_c) b_1^3 \tag{25}$$

and

$$\overline{G_2(\omega_a, \omega_b + \omega_c)} = \frac{1}{3}[G_2(\omega_a, \omega_b + \omega_c) + G_2(\omega_b, \omega_a + \omega_c) + G_2(\omega_c, \omega_a + \omega_b)].$$

3.3 *Volterra kernels for the collector-base junction capacitance and surface depletion capacitance*

These nonlinear capacitances can be represented as Taylor series expansions of the voltage δV_C across the capacitance.

$$C(\delta V_C) = C_0 + C_1\, \delta V_C + C_2 \delta V_C^2. \tag{26}$$

The current i_c through the capacitor can be expressed as

$$i_c = \frac{d}{dt}\left(C_0 \delta V_C + \frac{1}{2} C_1 \delta V_c^2 + \frac{1}{3} C_2 \delta V_C^3 \right). \tag{27}$$

Converting i_c to the frequency domain gives the Volterra series description

$$\delta I_c = j\omega\left(C_0 \delta V_C + \frac{1}{2} C_1 \delta V_C^2 + \frac{1}{3} C_2 \delta V_C^3 \right). \tag{28}$$

The depletion capacitance C_d can be found by differentiating the expression for charge in the depletion region (34) with respect to the surface potential. This procedure leads to the following expressions for the depletion capacitance Volterra kernels:

$$H_1(\omega) = j\omega \frac{dQ(0)}{dv} = -j\omega KH \tag{29}$$

where

$$H = \exp(u_s - u_{Fn}) - \exp(u_{Fp} - u_s) + 2 \sinh u_{Fn} \tag{29a}$$

$$K = \frac{qn_iL_D}{G^{1/2}} \tag{29b}$$

$$G = \exp(u_s - u_{Fn}) - \exp(-u_{Fn}) + \exp(u_{Fp} - u_s) - \exp u_{Fn} + 2u_s \sinh u_{Fn} \tag{29c}$$

and

$$L_D = \left[\frac{kT}{q}\frac{\epsilon_s}{2qn_i}\right]^{1/2}$$

$$H_2(\omega_1, \omega_2) = j(\omega_1 + \omega_2)\frac{K}{V_T^2}\left[\frac{H^2}{2G} - \exp(u_s - u_{Fn}) - \exp u_{Fp}\right] \quad (30)$$

$$H_3(\omega_1, \omega_2, \omega_3) = -\frac{K}{2V_T}\left\{\frac{3}{4}\frac{H^3}{G^2} - \frac{3}{2}\frac{H}{G}\right.$$

$$[\exp(u_{Fn} - u_s) + \exp(u_s - u_{Fp})] \quad (31)$$

$$\left. + \exp(u_s - u_{Fn}) - \exp(u_{Fp} - u_s)\right\},$$

where V_T is the thermal voltage kT/q.

3.4 Finding the dc solution for the MOS capacitor

Finding the dc solution for the MOS capacitor is simply a matter of finding the potential at the oxide-semiconductor interface corresponding to a prescribed dc bias voltage. The charges existing in the neighborhood of the interface can be expressed in terms of this surface (interface) potential. Since the entire MOS capacitor is electrically neutral, the summation of these charges must vanish. That is,

$$Q_g + Q_s + Q_{ss} + Q_o = F(\psi_s) = 0. \quad (32)$$

The charge on the gate Q_g is given by

$$Q_g = C_{ox}(V - \psi'_{MS} - \psi_s), \quad (33)$$

where V is the applied voltage, ψ'_{MS} the metal-semiconductor work function, ψ_s the surface potential, and C_{ox} the oxide capacitance.

The charge in the semiconductor (space-charge region) is given by Ref. 3:

$$Q_s = 2qn_iL_D[\exp(u_s - u_F) - \exp(-u_F) + \exp(u_F - u_s - v) - \exp(u_F - v) + 2u_s \sinh u_F]^{1/2}, \quad (34)$$

where u_s, u_F, and v are the surface potential, electron quasi-fermi potential, and applied voltage expressed in units of the thermal voltage kT/q.

The amount of charge in the surface states depends on the type of state (donor or acceptor), the surface state distribution, and the occupancy of the state as described by the fermi function. Figure 8 shows the charge on the surface states. We have made the conventional assumption that the states above mid-gap are acceptors and those

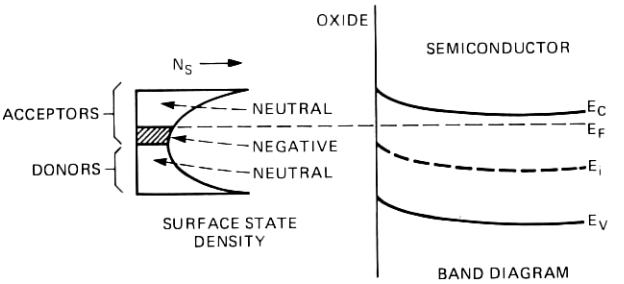

Fig. 8—Charge in surface states.

below mid-gap are donors.[8,9] Acceptors are negative and donors are neutral when filled by an electron. For simplicity, we have assumed that all states below the quasi-fermi level are occupied by electrons and all above are vacant. Thus the charge in the surface states Q_{ss} has been approximated by integrating the surface-state density N_s between u_F and u_s assuming all these states to be charged.

$$Q_{ss} = q\int_{u_F}^{u_s} N_s\, du, \tag{35}$$

Q_o is the fixed charge in the oxide.

The value of u_s which satisfies eq. (32) is the dc solution.

3.5 Computing circuit intermodulation

The modulation coefficient M_3 measured in decibels is defined by Ref. 10:

$$M_3 = 10 \log \frac{P_0(\omega_1 + \omega_2 - \omega_3)}{P_0(\omega_1)P_0(\omega_2)P_0(\omega_3)} - 15.6, \tag{36}$$

where P_0 is the output power measured in milliwatts for an input signal of the form

$$I_g = I_1 \cos \omega_1 t + I_2 \cos \omega_2 t + I_3 \cos \omega_3 t. \tag{37}$$

The perturbation method is used to compute the circuit response at the various combined frequencies as outlined below.

(*i*) Solve for the first-order response at ω_1 by replacing the nonlinear elements in the equivalent circuit (Fig. 7) with the first-order terms of the respective Volterra series, that is, $C_{d0}\, o\, \delta\psi_s$ for δi_d, $C_{j0}\, o\, \delta V_0$ for δi_j, and $D_1\, o\, \delta\psi_s$ for δi_s. The small signal response δV_0 is then computed for the resulting linear circuit for the input $I_1 \cos \omega_1 t$.

(*ii*) Solve for the first-order response at ω_2 and ω_3 in a similar fashion. Note that D_1 is frequency-dependent, so the first-order equivalent circuit is different for each frequency.

(*iii*) Solve for the second-order response at $\omega_1 + \omega_2$ by removing the I_g generator and inserting intermodulation current generators evaluated from the second-order terms in parallel with the linear-controlled current sources due to the first-order terms (see Fig. 9a). For example, for C_j an intermodulation generator of value $H_{j2} \; o \; \delta V_{02}^2$ shunts a capacitor of value C_{j0} and for δi_s an intermodulation generator $D_2 \; o \; \delta\psi_{s2}^2$ is in parallel with the linear generator $D_1 \; o \; \delta\psi_{s2}$, where both D_1 and D_2 are evaluated at $\omega_1 + \omega_2$. The second-order Volterra kernels require the values of the circuit node voltages at ω_1, ω_2, ω_3 computed in steps (*i*) and (*ii*).

(*iv*) Solve for the response at $\omega_1 - \omega_3$ and $\omega_2 - \omega_3$, as in step (*iii*).

(*v*) Solve for the response at $\omega_1 + \omega_2 - \omega_3$. The second-order intermodulation generators used in steps (*iii*) and (*iv*) are replaced by third-order intermodulation generators (see Fig. 9b). Each third-order generator consists of a pure third-order term plus three second-order interaction terms computed from the responses at $\omega_1 + \omega_2$, $\omega_1 - \omega_3$, $\omega_2 - \omega_3$, ω_1, ω_2, ω_3.

There are two kinds of contributors to the third-order generator currents. The first kind expresses the interaction of a second-order product with a fundamental signal to produce a third-order product [eq. (8)]. The second kind expresses the interaction of three fundamental signals to form a third-order product [eq. (9)]. In terms of

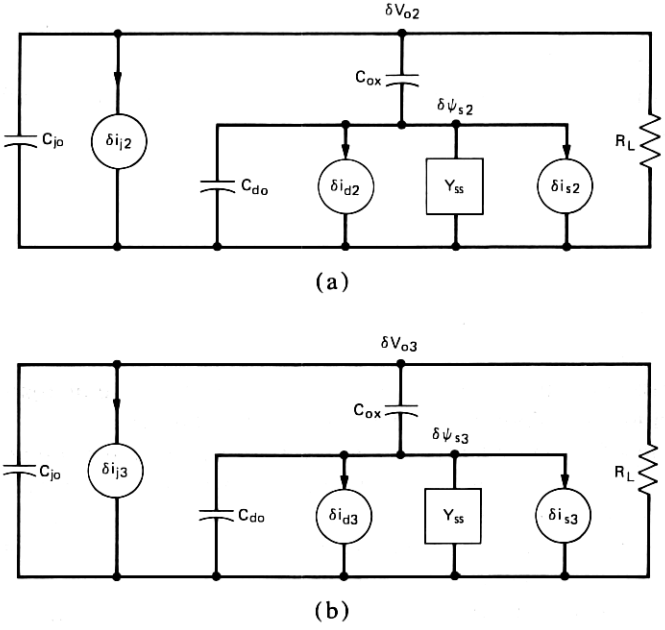

Fig. 9—Equivalent circuits for distortion analysis. (a) Circuit for finding second-order voltages. (b) Circuit for finding third-order voltages.

the output voltages in volts across load resistor R_L, M_3 becomes

$$M_3 = 20 \log \frac{|\delta V_{03}(\omega_1 + \omega_2 - \omega_3)| 2 \times 10^{-3} R_L}{|\delta V_{01}(\omega_1)\| \delta V_{01}(\omega_2)\| \delta V_{01}(\omega_3)|} - 15.6. \quad (38)$$

The output voltages found in steps (*i*), (*ii*), and (*v*) above are inserted into (38) to find the value of M_3.

IV. DETERMINING SURFACE PARAMETERS

Several parameters are used in this model to characterize the oxide-semiconductor interface. These describe:

(*i*) The distribution of surface states across the semiconductor bandgap.
(*ii*) The capacitance per unit area of the oxide.
(*iii*) The impurity concentration at the surface of the semiconductor.
(*iv*) The electron capture coefficient of the surface states.
(*v*) The fixed charge density in the oxide.

Although for these parameters the literature provides order-of-magnitude values that are representative of this kind of interface, some values are strongly dependent on the specific processing used to grow the oxide. This is particularly true of the surface-state distribution. Techniques for measuring surface-state distribution can be found in the literature. The surface-state density can be inferred, for example, from measurements of the ac conductance of an MOS capacitor.[6]

Measurements of capacitance and conductance were available for MOS capacitors fabricated with the identical oxidation process used for the transistors. These data covered wide ranges of frequency (0.1, 1, 5, 10, and 30 MHz) and bias voltage (from 0 volts into inversion). If appropriate values of the parameters were used, the ac and dc surface model developed for the intermodulation analysis should be able to predict these measurements quite accurately. An optimization program has been used to adjust the parameter values in this model to make it fit the measured admittance data. The surface-state density has been represented by a sixth-degree power series and each of the other parameters by a single average value.

Two small additions had to be made to the equivalent circuit of Fig. 7 to achieve a good fit of the data. A conductance was added in shunt with the oxide capacitance, and a series resistance was inserted at one of the terminals.

The fitting of the data required the use of an adaptive nonlinear least-squares algorithm.[11] A set of 12 parameters, seven of which characterized the surface-state distribution, were optimized by the algorithm. A thirteenth parameter, the electron capture cross section,

was held fixed at 5×10^{-16} cm^2. Figures 10 and 11 show the fitting of the conductance and capacitance data for the ⟨111⟩-oriented capacitors by the model. Figures 12 and 13 show the fitting for ⟨100⟩-oriented capacitors. The surface-state distributions resulting from this data fitting appear in Fig. 14; the rest of the parameters are listed in Table I. The surface-state distributions of Fig. 14 appear somewhat higher and have narrower valleys than is usually found for SiO_2-Si interfaces. It is known that the deposition of SiN layers over the SiO_2 layers can modify the surface-state distributions in this fashion.[12]

The values of oxide conductance in Table I are quite consistent with recently reported oxide conductance measurements of T. M. Nazar.[13] Although the frequency range of Nazar's measurements was below ours, his measurements show the conductance to be roughly proportional to frequency over a wide range. From this behavior, he suggests that the conductance is due to a hopping process of conduction. However, no mention was made of the orientation of his silicon substrates. In our model, it would probably have been better to

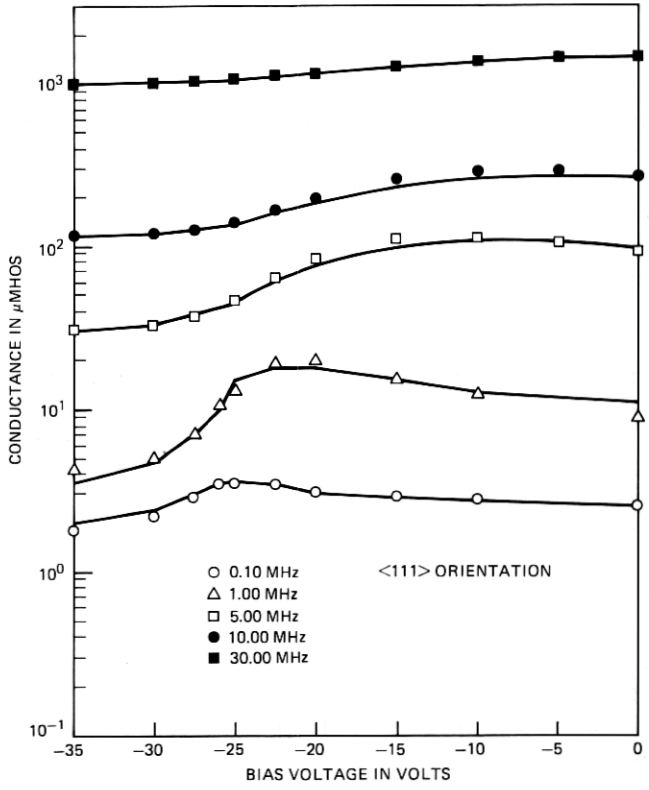

Fig. 10—Conductance of MOS capacitor.

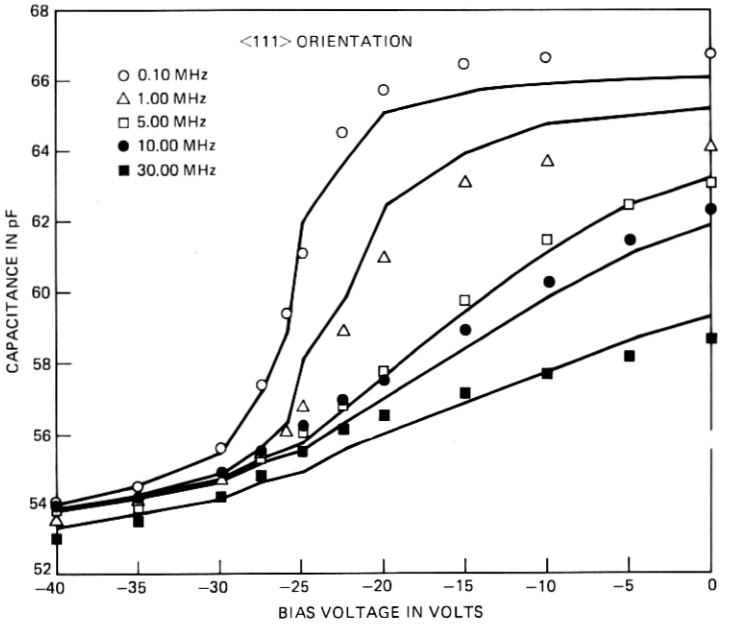

Fig. 11—Capacitance of MOS capacitor.

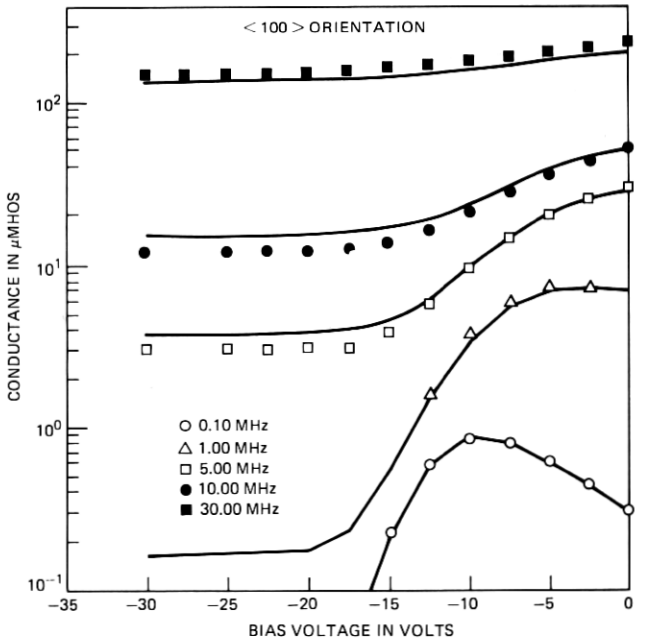

Fig. 12—Conductance of MOS capacitor.

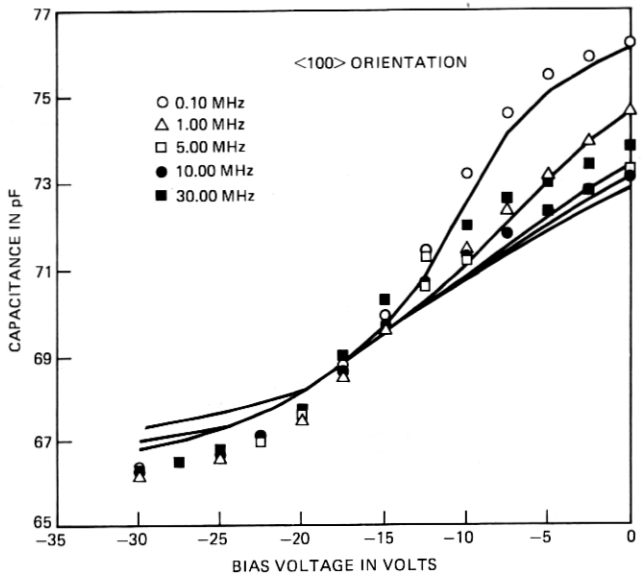

Fig. 13—Capacitance of MOS capacitor.

represent the conductance by a simple frequency dependence than to assume it to be constant, as we did. In any case, this has little effect on the computed modulation coefficient.

V. DISCUSSION OF RESULTS OBTAINED WITH THE COLLECTOR-BASE JUNCTION-CONTROLLED MOS CAPACITOR MODEL

Using the algorithms described above, values of M_3 have been computed for two collector-base junctions, each with a different junction-controlled MOS capacitor. These capacitors are characterized by the parameters given in Table I, which are representative of two different silicon crystal orientations, ⟨111⟩ and ⟨100⟩, with high and low surface-state densities. The collector doping profile of the SG transistor is far from flat near the collector-base junction. Hence, to find the junction capacitance, we preferred to use an algorithm that could calculate junction capacitance for an arbitrary doping profile. H.J.J. De Man has described a fast algorithm for such a calculation.[14] The algorithm used in this model for the collector-base junction capacitance is based on De Man's work.

R_D turned out to be more than two orders of magnitude smaller than R_s for these simulations and so was ignored. Moreover, in (22) $\delta\psi_{Fn}$ was assumed to be negligible in comparison with $\delta\psi_s$.

Computed and measured values of M_3 as a function of collector-base bias voltage are plotted in Figs. 15 and 16. Figure 15 represents the case of ⟨111⟩ crystal orientation, and Fig. 16 represents ⟨100⟩. The

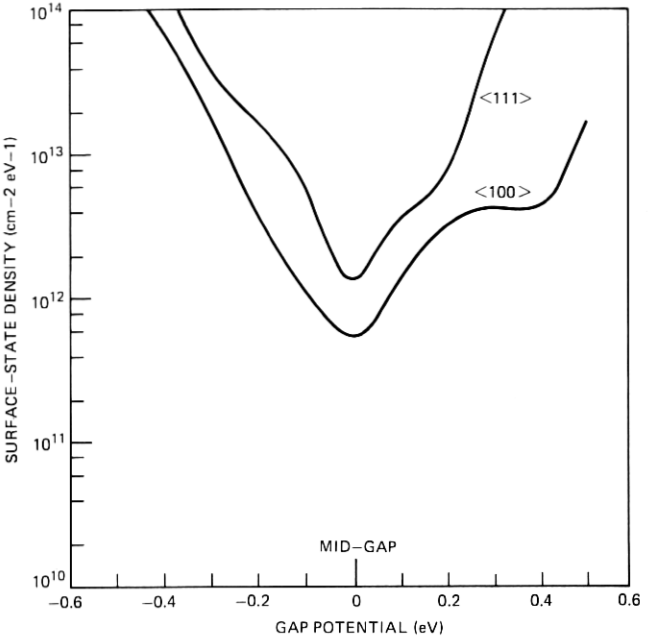

Fig. 14—Distribution of surface states.

Table I—Values of surface parameters

Parameter	Orientation ⟨111⟩	⟨100⟩
Oxide capacitance per unit area, nF cm^{-2}	3.83	4.19
Surface impurity concentration, $10^{15}cm^{-3}$	1.08	4.67
Fixed charge density, $10^{11}/cm^2$	5.85	3.15
Oxide conductance, micromhos/cm^2	75.	0.32
Series resistance, ohms	17.	1.6

computed curve for the ⟨111⟩ junction agrees qualitatively with the measured data in that it shows the hump that is characteristic of ⟨111⟩ junctions. The appearance of the hump at higher voltage in the computed curve than in the measured data is, we believe, due to inaccuracies in determining the surface parameters used for the simulation and to approximations used in the modeling.

The position and height of the hump are sensitive to the values of fixed charge and average surface-state density used in the simulation, as shown in Fig. 17. Even though the MOS capacitors used to determine the surface parameters all came from a single ⟨111⟩-oriented silicon slice and a single ⟨100⟩ slice, there was considerable variation in the measured admittance data for the ⟨111⟩ samples. This, in turn, produces a spread in the surface-state parameters derived from fitting the

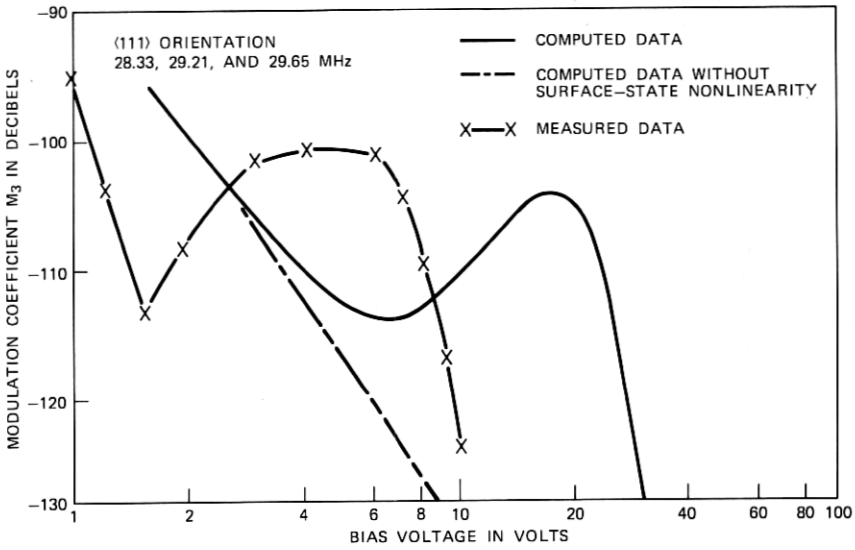

Fig. 15—Intermodulation characteristic.

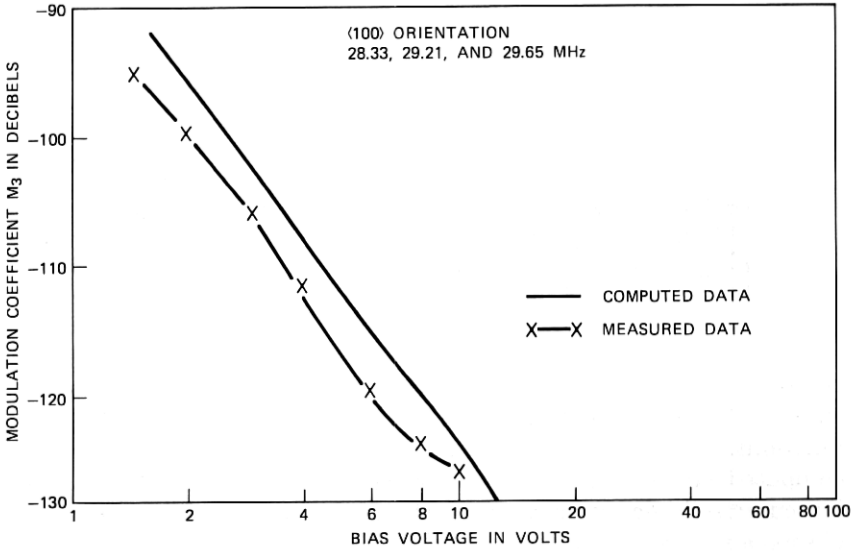

Fig. 16—Intermodulation characteristic.

admittance data. And this spread undoubtedly contributes to the difference between the computed and measured M_3.

As discussed earlier, the dominant surface effect on intermodulation would be expected to arise from the region under the base connecting pad. And so we have restricted our surface modeling to this portion of

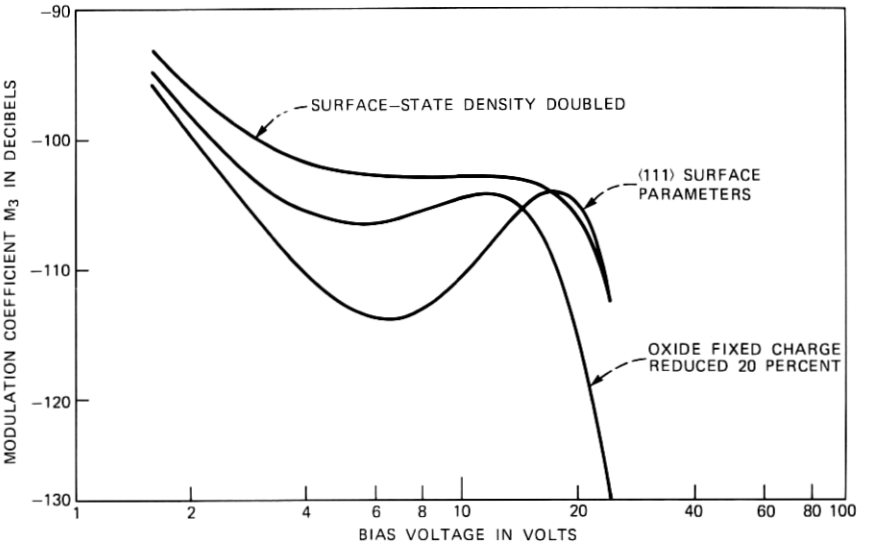

Fig. 17—Effects of changing surface parameters on intermodulation characteristic.

the intersection of the collector-base junction with the surface. However, there are probably also contributions from the extensive region not under the base pad where the collector-base junction intersects the surface. This region would be much more difficult to model, and we have not attempted to do so. This omission is probably responsible for some of the difference in the computed and measured M_3, also.

The computed M_3 for the ⟨100⟩ orientation agrees well with measured data. Note the almost complete absence of a hump in these curves. This is because of the low surface-state and fixed charge densities for this orientation.

If, in computing M_3, for the ⟨111⟩ case, the surface-state nonlinearity is omitted, the computed M_3 comes out to be that shown by the dashed line in Fig. 15. This shows clearly that the surface states are the primary source of the difference in intermodulation produced by the ⟨100⟩ and ⟨111⟩-oriented transistors.

Contour maps of M_3 in the f_1, f_2 frequency plane for a fixed value of the product frequency ($f_1 + f_2 - f_3$) reveal those combinations of frequency that give rise to high intermodulation. These maps have been computed using the collector-base junction-controlled MOS capacitor model. Figures 18 and 19 show M_3 maps for the ⟨111⟩ junctions at bias voltages corresponding to the peaks of the characteristic M_3-bias humps (see Fig. 15). These bias points (17 V for the simulation and 5 V for the measurements) have been chosen because surface effects dominate the distortion at these points. The predicted levels of M_3 and the general shape of the contours agree reasonably with

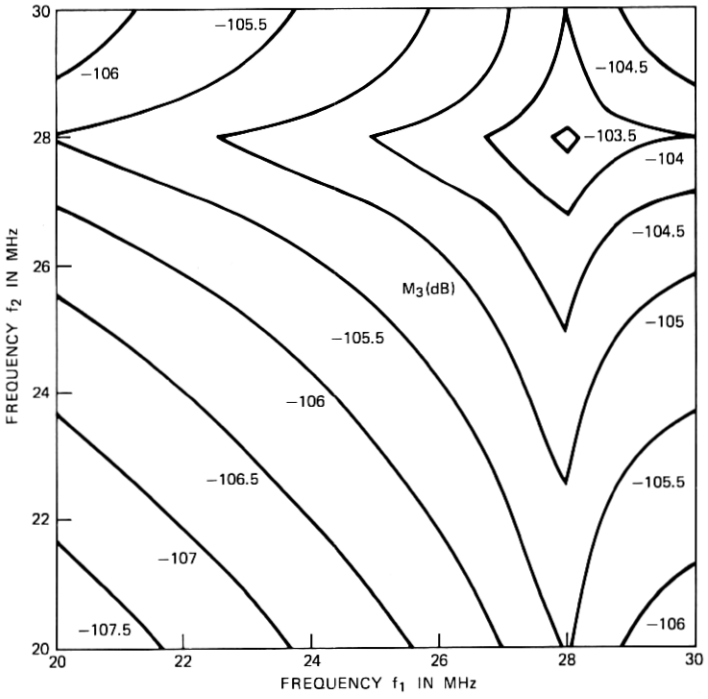

Fig. 18—Computed contour map of modulation coefficient.

measurements. However, the measurements show a stronger frequency dependence.

Contour maps of M_3 for ⟨100⟩ junctions are shown in Fig. 20 for the model and Fig. 21 for measured data. In the absence of any hump in the M_3-bias curves, a bias voltage of 5 V was chosen for the comparison. Again the predicted map agrees in magnitude and general shape with the measured map. The M_3 is seen to be less frequency-dependent than for the ⟨111⟩ case, except at frequencies very close to the product frequency.

It should be pointed out that the nonlinear model only includes terms up to third order. This approximation is valid only if the power in the fundamental driving tones is sufficiently low. The measured data shown in Figs. 15, 16, 19, and 21 have been measured with power in each fundamental P_0 set at −5 dBm. Lower power was not used because the resulting distortion power is near the test set noise limit of −140 dBm when the bias voltage is near 5 V. The power dependence of M_3 is shown in Fig. 22 for both ⟨111⟩ and ⟨100⟩ crystal orientations for a bias voltage of 5 V.

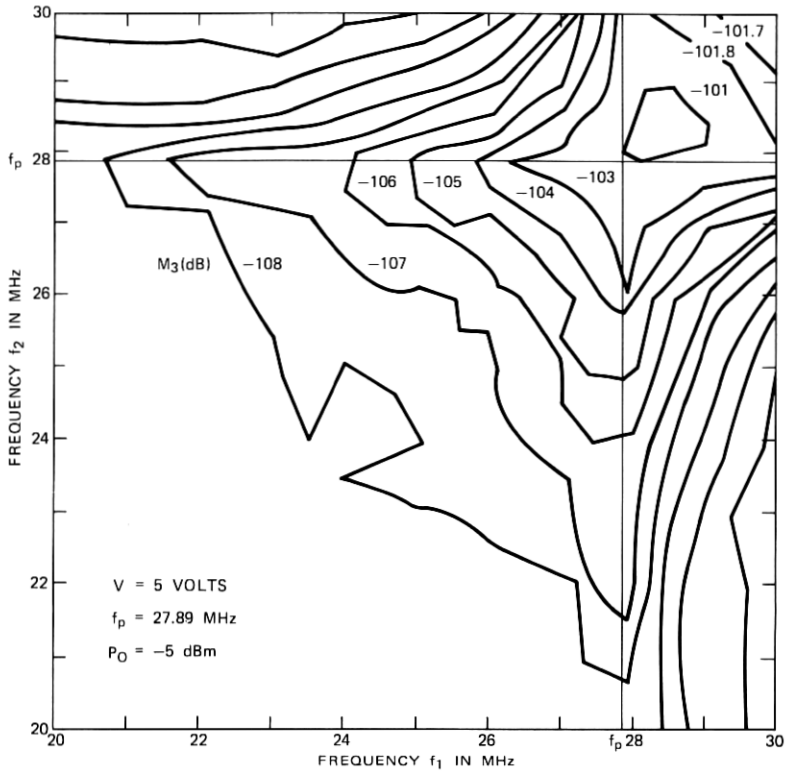

Fig. 19—Measured M_3 frequency map for ⟨111⟩ collector-base junction.

The noticeable rise in M_3 as P_0 is reduced indicates that the distortion mechanism is not accurately described by only second- and third-order terms when P_0 is greater than −15 dBm. This is because a pure third-order nonlinearity does not yield a power-dependent M_3. For this reason, the model of the collector-base junction does not predict M_3 variation with power. The lack of higher-order terms in the model may also explain the low predicted sensitivity of M_3 to the choice of fundamental frequencies.

The use of Volterra series and the perturbation method to describe a complex nonlinear system becomes rather unwieldly when terms higher than third-order are included. A simpler analytical method is needed to simulate the higher-order nonlinear effects in a collector-base junction-controlled MOS capacitor. Simulations using the present model suggest that the dominant source of surface-state distortion is due to the exponential dependence of surface electron density n_s on surface potential ψ_s as given in eq. (20). The G_2 and G_3 Volterra kernels are negligible contributors to the D_1, D_2, and D_3 composite Volterra kernels. If a higher-order nonlinear model were to be developed for

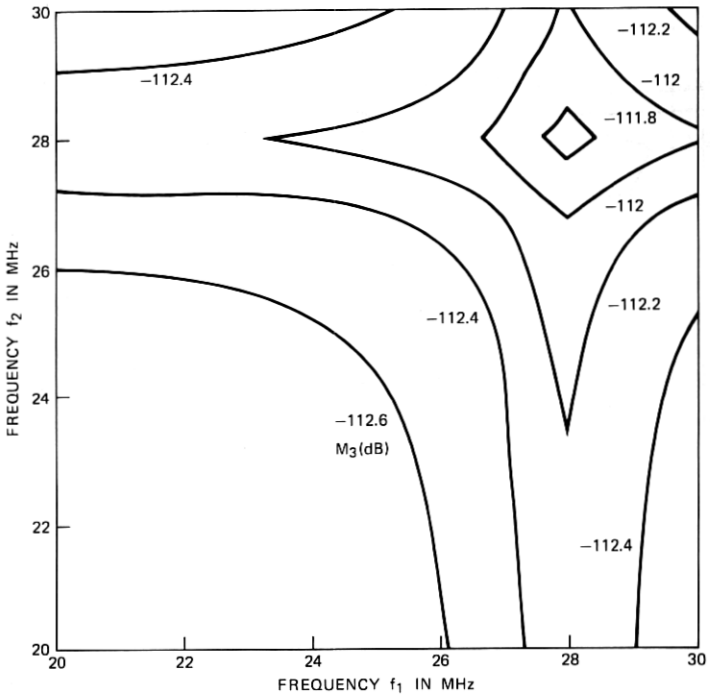

Fig. 20—Computed contour map of modulation coefficient.

surface-state intermodulation, perhaps only the n_s nonlinearity would need to be included.

These computations have shown how important the contribution of surface states can be to the nonlinear performance of collector-base junctions. If intermodulation distortion is critical in the application of these junctions, it is important to control the distribution of surface states at the Si-SiO_2 interface. This is not only a matter of the choice of crystal orientation, but a matter of the oxidation process used and also of post-oxidation processing.

VI. MODELING INTERMODULATION DISTORTION IN THE COMPLETE SG TRANSISTOR

Transistor models used in circuit analysis programs such as the Gummel-Poon model[15] and Extended Ebers-Moll model[16] are adequate for low-current modeling where temperature effects, base pushout, and lateral spreading are not important. Low-current operation means that, for a fixed collector-emitter voltage, the collector current is below the currents for which f_T or β peak. High-frequency circuits require

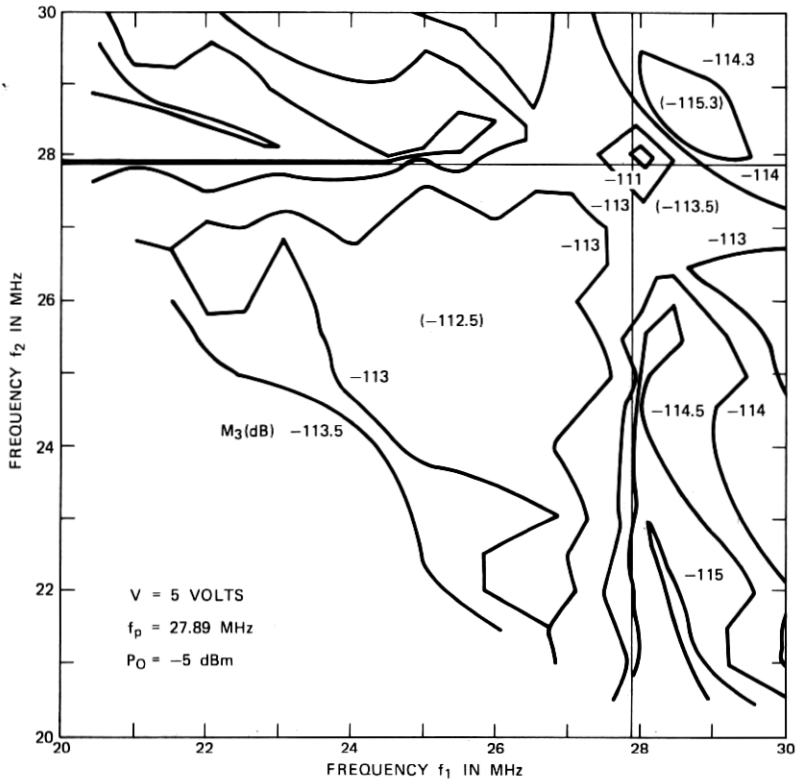

Fig. 21—Measured M_3 frequency map for ⟨100⟩ collector-base junction.

the highest f_T possible for the critical transistors, so the transistors must be biased with high currents.

The high current model presented in this paper extends the Gummel-Poon model by defining two base charge terms. One is the actual base charge and the other is a pseudo-base charge that allows Gummel's equation to describe the dominant component of collector current even when two-dimensional effects are important. In the limiting case of a one-dimensional structure, both charges are identical.

A number of high-current base-charge models have been proposed,[17-20] but they are based on device physics and need device geometry and material parameters as inputs. These models handle one-dimensional high current effects accurately, but only approximate two-dimensional effects. The base charge and the pseudo-base charge discussed in this paper are not derived from device physics but use empirical formulas as first suggested by Choma.[21] The equations for base charge given by Choma are found to model the quasi-base charge adequately, but a new set of equations is used to model the total base charge.

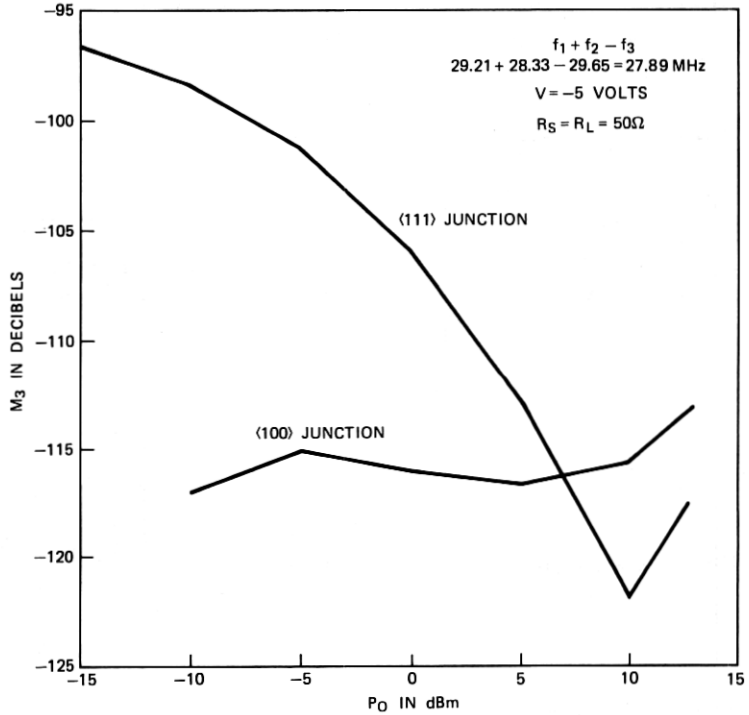

Fig. 22—Measured M_3 vs fundamental power for collector-base junctions.

Model parameter extraction is done with a computer program that uses measured currents and voltages of the test transistor as an input. A two-pass operation is needed to get a complete model. The first pass computes low current model parameters and plots the base charge multiplication factor. The user must define a functional form that can approximate the base charge multiplication factor as a function of collector current and collector-base voltage. The functional form may differ between transistor types due to different doping and structure. The user then computes initial guesses at the model parameters. The second pass uses an optimization program to refine the approximate model parameters. The use of a model parameter extraction program insures unique model parameters because the parameters are determined in precisely the same order with the same assumptions for every extraction run.

6.1 Transistor model description

The cross section of a typical bipolar device is shown in Fig. 23. Two components of dominant collector current I_{CCI}, I_{CCS} and base charge

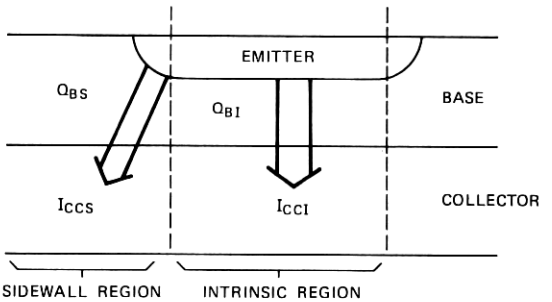

Fig. 23—Transistor cross section.

Q_{BI}, Q_{BS} associated with the intrinsic region directly under the emitter and the sidewall region are defined. The intrinsic region has current flow in only one dimension, and Gummel's equation applies where

$$I_{CCI} = \frac{I_S Q_{B0}[\exp(V_{BE}/V_T) - \exp(V_{BC}/V_T)]}{Q_{BI}}. \quad (39)$$

Of course, this assumes that lateral base current flow has a negligible effect. Current flow in the sidewall region is two-dimensional, and no rigorous analog of Gummel's equation exists to describe I_{CCS}. However, if one sacrifices rigor, (39) can be modified to approximate I_{CC}.

$$I_{CC} = I_{CCI} + I_{CCS} = \frac{I_S Q_{B0}[\exp(V_{BE}/V_T) - \exp(V_{BC}/V_T)]}{Q_{BQ}}, \quad (40)$$

where Q_{BQ} is defined as the quasi-base charge which equals Q_{BI} for a purely intrinsic device. At low collector currents, $Q_{BQ} \approx Q_{BI}$. However, at high currents both base pushout and lateral spreading occur, and Q_{BQ} must change; so (40) models $I_{CCI} + I_{CCS}$. Q_{BQ} can be expressed as shown below.

$$Q_{BQ} = Q_{B0}\left[1 + \frac{Q_E}{C_{JE0}V_{B0}} + \frac{Q_C}{C_{JC0}V_{A0}} + \frac{T_{F0}}{Q_{B0}} B_X(V_{BE}, V_{BC}) I_{CC}\right] \quad (41)$$

Q_{B0} = approximate zero bias total majority base charge
Q_E = base-emitter junction majority charge
Q_C = base-collector junction majority charge
V_{A0} = forward Early voltage
V_{B0} = reverse Early voltage
T_{F0} = extrapolated low-current transit time for $V_{CB} = 0$
$B_X(V_{BE}, V_{BC})$ = base pushout and lateral spreading function.

For an intrinsic device, $C_{JE0}V_{B0} = C_{JC0}V_{A0} = Q_{B0}$. However, this is not

true for a real two-dimensional device. The emitter junction charge Q_E and the associated capacitance C_E are given below.

$$Q_E = \int_0^{V_{BE}} C_E(V)\, dV \tag{42}$$

$$C_E = \begin{cases} C_{E\max} & V_{BE} > P_E(1 - B_E) \\ C_{JE0}\left(\dfrac{V_{BE}}{P_E}\right)^{-M_E} & V_{BE} < P_E(1 - B_E) \end{cases} \tag{43}$$

$$B_E = \left(\frac{C_{JE0}}{C_{E\max}}\right)^{1/M_E}. \tag{44}$$

The zero-bias capacitance is C_{JE0}, whereas the peak value of the depletion capacitance in forward bias is $C_{E\max}$. B_E defines the voltage at which C_E becomes constant at $C_{E\max}$, and P_E is the built-in voltage. The collector charge and capacitance are defined with similar equations and model parameters C_{JC0}, P_E, M_C. An empirical function for B_X is described by Choma[21] and is given below:

$$B_X(V_{BE}, V_{BC}) = B_{X0} + (1 - B_{X0})e^{-f} \tag{45}$$

$$B_{X0} = 1 + ae^{V_{BC}/b} \tag{46}$$

$$f = c(e^{V_{BE}/d} - 1), \tag{47}$$

where a, b, c, and d are model parameters.

This function is adequate for test devices studied in this paper, but other functions may be necessary for different device structures.

Equation (41) defines Q_{BQ} in terms of I_{CC}; to define Q_{BQ} in terms of only V_{BE} and V_{BC}, substitute (40) into (41) and solve for Q_{BQ} to get

$$\frac{Q_{BQ}}{Q_{B0}} = \frac{1}{2}\left(1 + \frac{Q_E}{C_{JE0}V_{B0}} + \frac{Q_C}{C_{JC0}V_{A0}}\right) + \frac{1}{2}\left[\left(1 + \frac{Q_E}{C_{JB0}V_{B0}} + \frac{Q_C}{C_{JC0}V_{A0}}\right)^2 + \frac{4T_{F0}}{Q_{B0}} B_X I_S\left(e^{V_{BE}/V_T} - e^{V_{BC}/V_T}\right)\right]^{1/2}. \tag{48}$$

The base-pushout and lateral spreading function B_X as defined by (45), (46), and (47) is only valid for the active or quasi-saturation regions of operation. A more complete description of B_X is needed to model inverse operation.

The description of I_{CC} given above is combined with the other elements of the Gummel-Poon model[15] to describe base current and charge storage as shown in Fig. 24. The base currents injected into the collector I_{BC} and emitter I_{BE} and the base resistance R_B are given by

$$I_{BE} = I_1 e^{V_{BE}/V_T} + I_2 e^{V_{BE}/N_E V_T} \tag{49}$$

$$I_{BC} = I_3 e^{V_{BC}/V_T} + I_4 e^{V_{BC}/N_C V_T} \tag{50}$$

$$R_B = R_{BX} + R_{BI}/(Q_{BQ}/Q_{B0}). \tag{51}$$

The base resistance due to the external base is modeled with a constant resistance R_{BX} and a conductivity-modulated resistance R_{BI}.

Self-heating of a device is an important consideration for high-current modeling, so an auxiliary model is included. A current generator equal to the power being dissipated in the device drives the thermal resistance R_T and capacitance C_T. The voltage across R_T equals the instantaneous temperature of the device. For low-frequency circuit simulations, the temperature of the device must be included as a dynamic variable in all the model equations. However, for high frequency simulations, only the dc operating point must be computed with temperature as a variable, since the time constant of the $R_T C_T$ network is long.

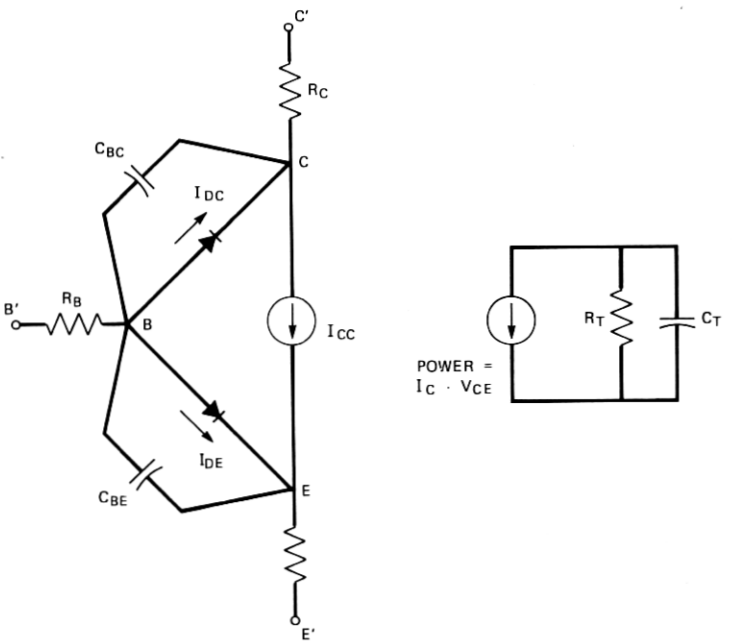

Fig. 24—Transistor model topology.

Charge storage is modeled by capacitors C_{BE} and C_{BC} where

$$C_{BE} = \frac{\partial Q_B}{\partial V_{BE}}, \qquad C_{BC} = \frac{\partial Q_B}{\partial V_{BC}} \tag{52}$$

and Q_B is the actual charge in the base not to be confused with Q_{BQ}. This definition of C_{BE} and C_{BC} assumes the quasi-static approximation[22] for charge distributions in the base. The base charge distribution at time t_0 is given by the dc charge distribution evaluated for $V_{BE} = V_{BE}(t_0)$ and $V_{BC} = V_{BC}(t_0)$. The excess phase in the β versus frequency measurement is caused by delay in the base and in the collector space-charge regions. The quasi-static approximation does not model the diffusion of carriers in the base or drift of carriers in the space-charge region; hence, excess phase is not modeled. However, at frequencies that are low compared to the f_T of the device, the quasi-static model is useful.

The actual base charge consists of a constant charge due to doping Q_{B0}, depletion charge Q_E, Q_C, and diffusion charge, and is defined in a similar fashion as Q_{BQ} to be

$$Q_B = Q_{B0} + Q_E + Q_C + T_{F0}B_Y(I_{CC}, V_{BC})I_{CC}. \tag{53}$$

Note that Q_{B0} is not really necessary in (53) since only the derivatives of Q_B are used. The function $B_Y(V_{BE}, V_{BC})$ accounts for the effects of base pushout and lateral spreading. It is necessary to use a different functional form for B_Y than used for B_X. The f_T vs I_C data cannot be matched closely at both low and high V_C if B_Y has the same form as B_X. However, with B_Y given by the function in (54), the f_T data could be matched over the entire range of V_{CB} as shown in Fig. 25. The dc β vs I_C curve corresponding to Fig. 25 is shown in Fig. 26.

$$B_Y = AI_{CC}^n + B_{Y0} \tag{54a}$$

$$n = 1 + n_0 e^{-I_C/n_1} \tag{54b}$$

$$B_{Y0} = B_1 e^{V_{BC}/B_2} + B_3 \tag{54c}$$

$$A = A_1 V_{BC}^2 + A_2 V_{BC} + A_3 \tag{54d}$$

$$n_0 = C_1 + C_2 V_{BC} \tag{54e}$$

$$n_1 = C_3 + C_4 V_{BC} \tag{54f}$$

with model parameters A_1, A_2, A_3, B_1, B_2, B_3, C_1, C_2, C_3, C_4. Equation (54) represents a function of considerable complexity. However, each subfunction (54b) to (54f) is determined from plots of A, n, and B_{Y0} vs V_{BC} obtained from measured data. The exact forms of these equations may differ for devices with completely different structures.

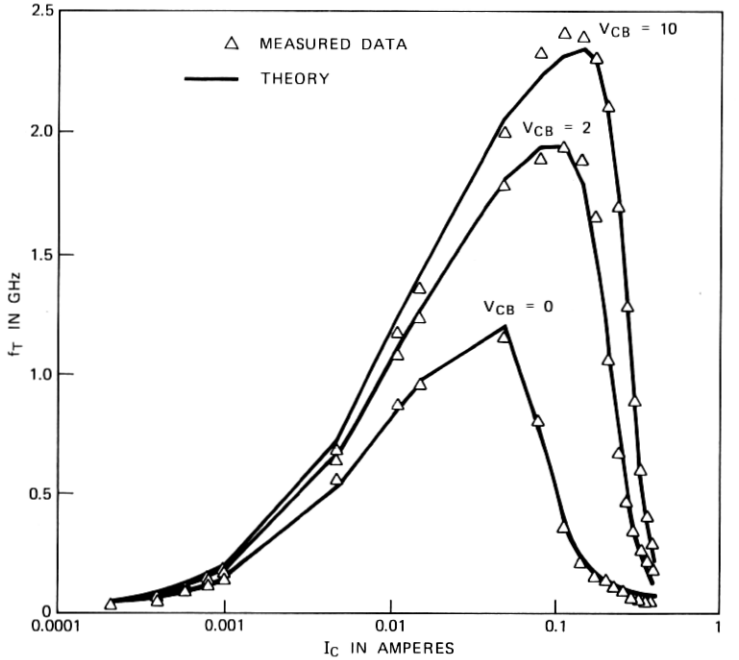

Fig. 25—f_T-current characteristics.

VII. COMPUTATIONS USING THE TRANSISTOR MODEL

The SG transistor has been the product of years of effort to develop a highly linear transistor for submarine cable use.[23,24] As a result, extreme flatness of the I_{BE} versus V_{BE} and β versus V_{BC} and I_C characteristics has been achieved.[23,24]

We have tried to model the SG transistor carefully, so that the model would reproduce measured distortion accurately when anomalous distortion is absent. However, in this attempt, it has become apparent that the distortion predicted by the transistor model per se without surface effects has been excessive.

The primary source of the excess transistor distortion from the model is its inability to adequately simulate the extreme linearity of the SG transistor. To accomplish this involves fitting not only f_T and β accurately over a wide range of voltage and current bias, but the second and third derivatives of these quantities as well. Poon[24] has shown that, in the high frequency, limit M_3 is strongly related to the second derivative of f_T. At lower frequencies, β becomes important. Unfortunately, the modeling equations are not capable of matching β and f_T over a wide bias range. To improve the model, the functions

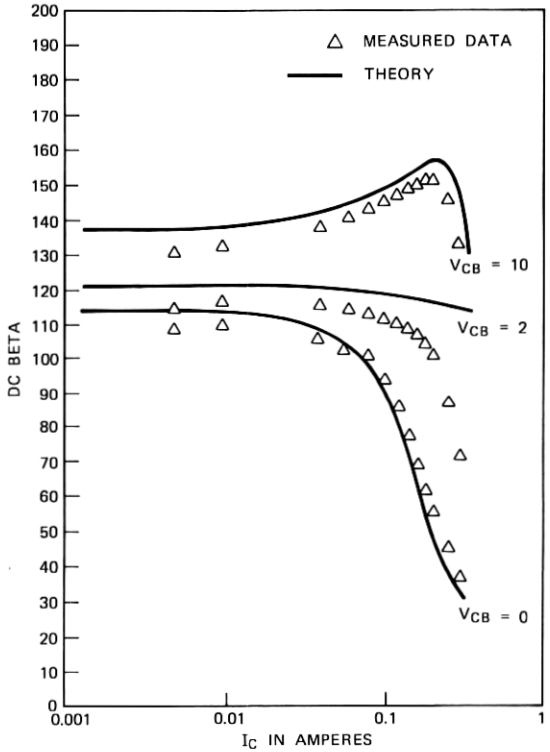

Fig. 26—Direct-current beta-current characteristics.

describing base charge B_X (47) and B_Y (54) must be increased in complexity so as to fit the higher derivatives of charge.

Replacing the collector-base diode with the full transistor model produced no fundamentally new problems to the intermodulation computation itself. The principal effect was simply to increase the complexity of the computations as a result of the increase in equivalent circuit complexity.

Intermodulation analysis requires derivatives up to third order for all nonlinear elements. These are easily obtained explicitly except for the normalized base charge Q_B, which is a function of V_{BE} and V_{BC}. Derivatives of Q_B have been computed numerically to avoid derivation mistakes and to allow quick changes in the equations for Q_B without rederiving the derivatives.

For an operating bias of V_{CB} = 10 V, the internal junction temperature is elevated about 75°C. The inclusion of junction heating in the transistor model lowers the simulated M_3 by some 4 dB at the higher voltages. This occurs because of the slight reduction of exponential modeling factors of the form $e^{qV/kT}$.

Computed and measured plots of M_3 versus collector-base bias are shown in Fig. 27. The measured data show the characteristic hump for the ⟨111⟩-oriented transistor. These plots are very similar to those for just the collector-base junction (Figs. 15 and 16), the principal difference being that the transistor amplifies the distortion by about 10 dB.

For the simulated M_3 curve, the β transistor nonlinearities were artificially reduced in accordance with the comments above. Without this reduction, the M_3 curve from the transistor alone would be about 14 dB higher at the high-voltage end and would override any contribution from surface effects. The effect of the surface-state contribution to M_3 is seen to be a hump at approximately the same level as the measured hump.

Although the transistor model does not allow exact prediction of

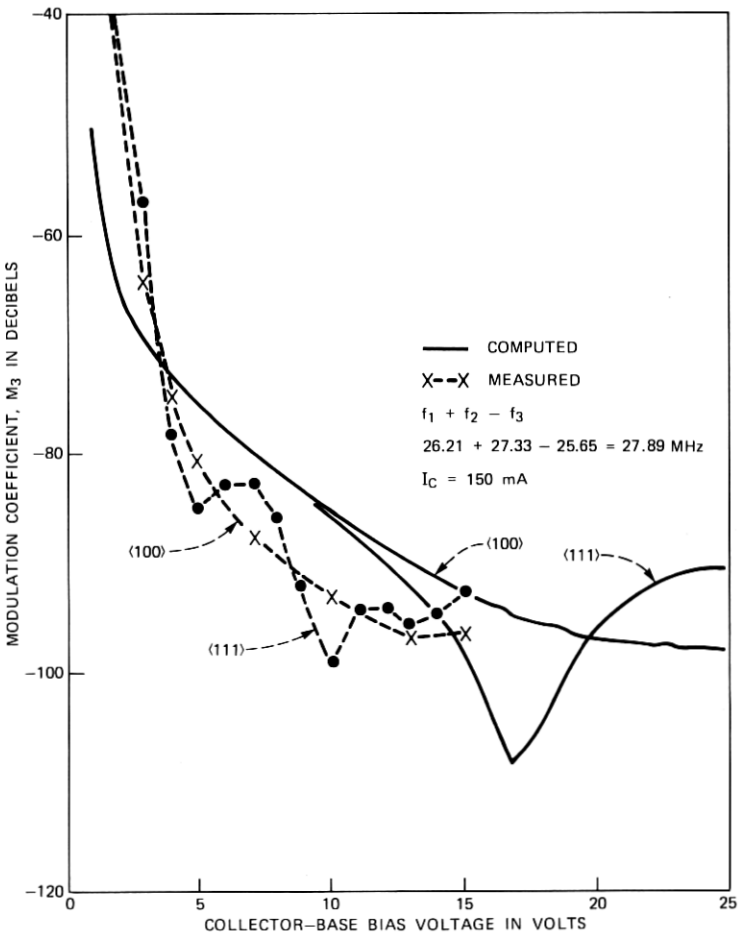

Fig. 27—Transistor intermodulation-voltage characteristics.

distortion, simulations were made to show variations of M_3 with collector current. As shown in Fig. 28, these follow the same trend as measured data. The general shape of the curves is a result of transistor nonlinearities, not surface effects. Base current is composed of two terms.

$$I_B = \frac{I_C}{\beta} + \frac{dQ_B}{dt}. \tag{55}$$

At high currents where β is constant, Q_B is dominated by depletion charge, which is nonlinearly related to I_C. As I_C increases, Q_B becomes dominated by diffusion charge, and Q_B is proportional to I_C/f_T. The first minimum in M_3 is reached at the current for which $\partial f_T/\partial I_C = 0$, that is, at the peak of the $f_T - I_C$ curve. The next local minimum in M_3

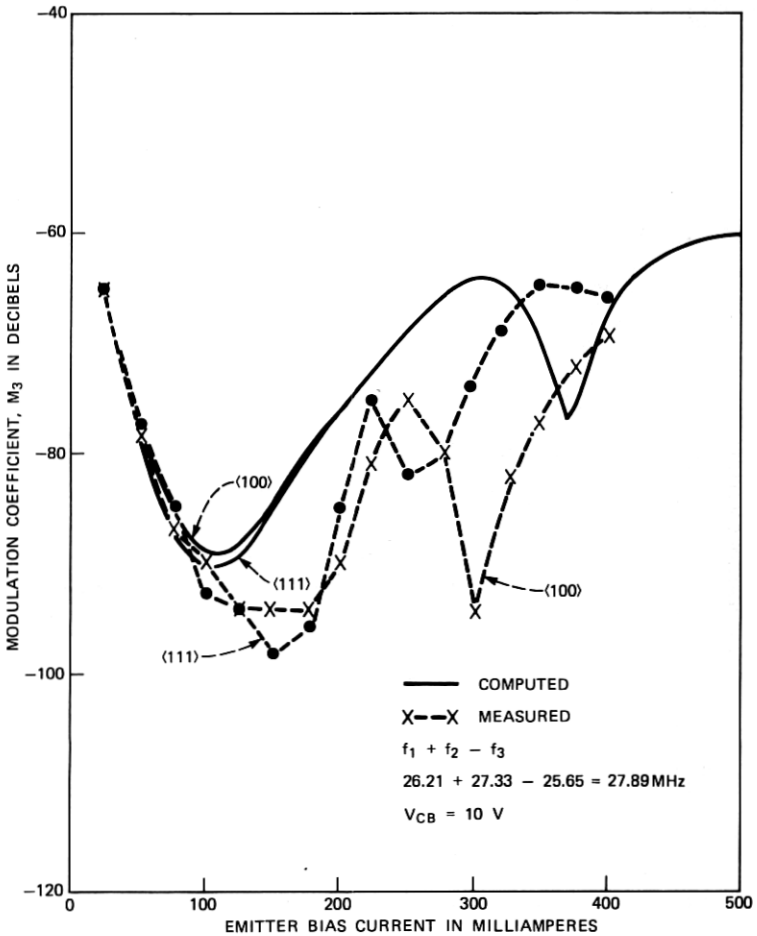

Fig. 28—Transistor intermodulation-current characteristics.

occurs where $\partial^2 f_T/\partial I_c^2 = 0$, that is, at the inflection point in the $f_T - I_C$ curve. This simplified discussion is valid at high frequency where dQ_B/dt dominates in (55). For lower frequencies, the effect of nonlinearities in β becomes important.

VIII. ACKNOWLEDGMENTS

We would like to express our appreciation to L. E. Miller for having originally proposed the hypothesis that surface effects are responsible for the anomalous SG distortion and for his enthusiastic support of this work. We are also indebted to D. G. Ross for making available to us his extensive collection of experimental intermodulation data. M. Chruney made the capacitance and conductance measurements on the MOS capacitors, which were provided by W. M. Fox. L. C. Kaufman supplied the algorithm for adjusting the model parameters to fit these measurements.

APPENDIX A

Integrating Volterra Kernels over the Surface-State Distribution

As can be seen from equation (19) and Appendix C, to find the total current flowing into the surface states involves a sum of integrals containing the factor

$$\frac{f_0(1 - f_0)}{1 + j\omega f_0/c_n n_{s0}}, \tag{56}$$

where $f_0 = [1 + g_s \exp(u - u_F)]^{-1}$.

Now

$$f_0(1 - f_0) = \frac{g_s \exp(u - u_F)}{[1 + g_s \exp(u - u_F)]^2} = \frac{df_0}{du} \tag{57}$$

is sharply peaked about $u = u_F$. This is readily seen by plotting $f_0(u)$ and noticing that it slopes steeply only near $u = u_F$. Since df_0/du is peaked, so are $f_0(df_0/du)$ and $f_0^2(df_0/du)$. If $\omega/c_n n_{s0} \ll 1$, that is, at low frequency and high semiconductor doping, (56) reduces approximately to (57). Therefore, provided that N_s is essentially constant through this peak, the integrals in (19) can be readily evaluated in the manner of Nicollian and Goetzberger.[7]

However, as $\omega/c_n n_{s0}$ becomes comparable with or greater than unity, i.e., at high frequency or low doping, the peak broadens and shifts away from u_F toward the conduction band. The location of the peak can be found by setting the derivative of (56) with respect to u equal to zero and solving for u. The integrals could then be evaluated as above with N_s taken out of the integral and set equal to the value at the peak location. But broadening the peak makes this approach rather

unpalatable, and we have preferred to evaluate the integrals numerically.

APPENDIX B

Taking into Account Surface Potential Fluctuations in Calculating Surface-State Volterra Kernels

Following Nicollian and Goetzberger,[7] assume that the dc surface potential is uniform over a small region of characteristic area α. The probability that the dc surface potential on a particular one of these regions lies between u_s and $u_s + du_s$ is $P(u_s)\ du_s$. Then, to find the first-order Volterra kernel $D_1(\omega_1)$, we multiply (23) by $P(u_s)\ du_s$ and integrate over all possible surface potentials.

$$\int_{-\infty}^{\infty} D_1(\omega_1)P(u_s)\ du_s = \int_{-\infty}^{\infty} j\omega_1 \frac{q}{V_T} \int_{u_V}^{u_C} N_s(u, u_s)H_1(\omega_1)\ du \cdot n_{s0}P(u_s)\ du_s. \quad (58)$$

We recognize that f_0 is not a function of u_s and assume $P(u_s)$ to be sharply peaked at the average surface potential $\bar{u}_s$. In particular, we assume $P(u_s)$ to be Gaussian.

$$P(u_s) = (2\pi\sigma_s^2)^{-1/2} \exp\left[\frac{-(u_s - \bar{u}_s)^2}{2\sigma_s^2}\right], \quad (59)$$

where

$$\sigma_s = \frac{A}{(C_{ox} + C_d)\ V_T}\left[\frac{q\bar{Q}}{\alpha(D_d)}\right]^{1/2}$$

and $\bar{Q}$ is the mean oxide charge density in C/cm^2.

Then inverting the order of integration, we assume that $N_s(u, u_s)$ varies slowly with u_s and can be taken outside the integral with respect to u_s. We then have

$$\int_{-\infty}^{\infty} D_1(\omega_1)\,P(u_s)\ du_s = \frac{j\omega_1 q}{V_T} \int_{u_V}^{u_C} N_s(u, \bar{u}_s)\, f_0(1 - f_0) \int_{-\infty}^{\infty} \frac{P(u_s)\ du_s}{1 + R(u_s)}\, du, \quad (60)$$

where $\bar{u}_s$ is the average value of the surface potential and

$$R(u_s) = \frac{j\omega_1 f_0}{c_n n_i} \exp\,[-(u_s - u_F)].$$

Now expand $[1 + R(u_s)]^{-1}$ in a Taylor's series about $\bar{u}_s$,

$$F(u_s) = \frac{1}{1 + R(u_s)} = F(\bar{u}_s) + F'(\bar{u}_s)(u_s - \bar{u}_s) + \frac{F''(\bar{u}_s)}{2}(u_s - \bar{u}_s)^2 + \cdots.$$

Then

$$\int_{-\infty}^{\infty} \frac{P(u_s)}{1+R(u_s)}\,du_s \approx F(\bar{u}_s)\int_{-\infty}^{\infty} P(u_s)\,du_s + F'(\bar{u}_s)\int_{-\infty}^{\infty}(u_s-\bar{u}_s)P(u_s)\,du_s + \frac{F''(\bar{u}_s)}{2}\int_{-\infty}^{\infty}(u_s-\bar{u}_s)^2P(u_s)\,du_s \approx F(\bar{u}_s)+\frac{\sigma_s^2}{2}F''(\bar{u}_s). \tag{61}$$

The second integral on the right vanishes. Hence,

$$\int_{-\infty}^{\infty} D_1(\omega_1)P(u_s)\,du_s = \frac{j\omega_1 q}{V_T}\int_{u_V}^{u_C} N_s f_0(1-f_0)\hat{F}_1(\omega_1,\bar{u}_s)\,du, \tag{62}$$

where $\hat{F}_1(\omega_1, \bar{u}_s)$ is the quantity on the right side of (61).

Treating the second- and third-order Volterra kernels similarly, we obtain

$$\int_{-\infty}^{\infty} D_2(\omega_1,\omega_2)P(u_s)\,du_s \approx -\frac{j(\omega_1+\omega_2)q}{2V_T^2}\int_{u_V}^{u_C}[\hat{F}_1(\omega_1+\omega_2,\bar{u}_s)f_0 - \hat{F}_2(\omega_1,\omega_2,\bar{u}_s)f_0^2]N_s(u)(1-f_0)\,du, \tag{63}$$

where, letting $\omega_1+\omega_2-\omega_3=\omega_p$,

$$\hat{F}_2(\omega_1,\omega_2,\bar{u}_s) = F(\omega_1,\omega_1+\omega_2,\bar{u}_s)+F(\omega_2,\omega_1+\omega_2,\bar{u}_s) + \frac{\sigma_s^2}{2}[F''(\omega_1,\omega_1+\omega_2,\omega_p,\bar{u}_s) + F''(\omega_2,\omega_1+\omega_2,\omega_p,\bar{u}_s)]$$

$$\int_{-\infty}^{\infty} D_3(\omega_1,\omega_2,\omega_3)P(u_s)\,du_s \approx -\frac{j(\omega_p)q}{V_T^3}\int_{u_V}^{u_C}\left[\frac{\hat{F}_1(\omega_p,\bar{u}_s)}{6}f_0 - \overline{\hat{F}_2(\omega_1,\omega_2+\omega_3,\bar{u}_s)}f_0^2 + \frac{\hat{F}_3(\omega_1,\omega_2,\omega_3,\bar{u}_s)}{6}f_0^3\right]\cdot(1-f_0)N_s(u)\,du, \tag{64}$$

where the bar is used as in (25) and

$$\hat{F}_3(\omega_1, \omega_2, \omega_3) = F(\omega_1, \omega_1 + \omega_2, \omega_p, \bar{u}_s) + F(\omega_2, \omega_1 + \omega_2, \omega_p, \bar{u}_s)$$
$$+ F(\omega_1, \omega_1 + \omega_3, \omega_p, \bar{u}_s) + F(\omega_3, \omega_1 + \omega_3, \omega_p, \bar{u}_s)$$
$$+ F(\omega_2, \omega_2 + \omega_3, \omega_p, \bar{u}_s) + F(\omega_3, \omega_2 + \omega_3, \omega_p, \bar{u}_s)$$
$$+ \frac{\sigma_s^2}{2}[F''(\omega_1, \omega_1 + \omega_2, \omega_p, \bar{u}_s)$$
$$+ F''(\omega_2, \omega_1 + \omega_2, \omega_p, \bar{u}_s)$$
$$+ F''(\omega_1, \omega_1 + \omega_3, \omega_p, \bar{u}_s) + F''(\omega_3, \omega_1 + \omega_3, \omega_p, \bar{u}_s)$$
$$+ F''(\omega_1, \omega_2 + \omega_3, \omega_p, \bar{u}_s) + F''(\omega_3, \omega_2 + \omega_3, \omega_p, \bar{u}_s)].$$

The definitions of F and F'' are as follows:

$$F(\omega_1, \omega_2, \cdots, w_n) = \prod_{i=1}^{n} \frac{1}{1 + R(\omega_i)}$$

$$F''(\omega_1, \omega_2, \cdots, \omega_n) = F(\omega_1, \omega_2, \cdots, \omega_n)$$
$$\left[\left(\sum_{i=1}^{n} R(\omega_i)F(\omega_i)\right)^2 - \sum_{i=1}^{n} R(\omega_i)F^2(\omega_i)\right].$$

APPENDIX C

Derivation of Surface-State Volterra Kernels

A Volterra series for f in terms of n_s, eq. (12), describing the time dependence of the Fermi level is rewritten as

$$\frac{df}{dt} = c_n(1 - f)n_s - e_n f. \tag{65}$$

First break (56) into a dc part and an ac part. Let

$$f = f_0 + \delta f, \qquad n_s = n_{s0} + \delta n_s$$

$$\frac{d}{dt}\delta f = c_n(1 - f_0 - \delta f)(n_{s0} + \delta n_s) - e_n(f_0 + \delta f).$$

Direct current equation:

$$0 = c_n(1 - f_0)n_{s0} - e_n f_0.$$

Therefore

$$e_n = \frac{c_n(1 - f_0)n_{s0}}{f_0}$$

or

$$\frac{c_n n_{s0}}{f_0} = c_n n_{s0} + e_n.$$

Alternating current equation:

$$\frac{d}{dt}\,\delta f = c_n(1 - f_0)\delta n_s - (c_n n_{s0} + e_n)\delta f - c_n \delta f \delta n_s$$

or

$$\frac{d}{dt}\,\delta f = c_n(1 - f_0)\delta n_s - \frac{c_n n_{s0}}{f_0}\,\delta f - c_n \delta f \delta n_s. \tag{66}$$

It is desirable to express δf as a Volterra series

$$\delta f = H_1(\omega_a) \circ \delta n_s + H_2(\omega_a, \omega_b) \circ \delta n_s^2 + H_3(\omega_a, \omega_b, \omega_c) \circ \delta n_s^3, \tag{67}$$

where the $\circ$ operator indicates that the magnitude and phase of each term in δn_s^n is to be changed by the magnitude and phase of $H_n(\omega_a, \cdots, \omega_n)$. To find the Volterra kernels $A_n(\omega_1, \cdots, \omega_n)$ substitute (58) into the ac eq. (57) using a theorem for higher order Fourier transforms of derivatives (76) to get:

$$\begin{aligned} j\omega_a H_1(\omega_a) \circ \delta n_s + j(\omega_a + \omega_b)H_2(\omega_a, \omega_b) \circ \delta n_s^2 \\ + j(\omega_a + \omega_b + \omega_c)H_3(\omega_a, \omega_b, \omega_c) \circ \delta n_s^3 \\ = c_n(1 - f_0)\delta n_s - \frac{c_n n_{s0}}{f_0}\,[H_1(\omega_a) \circ \delta n_s + H_2(\omega_a, \omega_b) \circ \delta n_s^2 \\ + H_3(\omega_a, \omega_b, \omega_c) \circ \delta n_s^3] \\ - c_n\{[H_1(\omega_a) \circ \delta n_s]\delta n_s + [H_2(\omega_a, \omega_b) \circ \delta n_s^2]\delta n_s \\ + [H_3(\omega_a, \omega_b, \omega_c) \circ \delta n_s]\delta n_s\}. \end{aligned}$$

Consider $\delta n_s = a_1 \cos(\omega_1 t + \phi_1) + a_2 \cos(\omega_2 t + \phi_2) + a_3 \cos(\omega_3 t + \phi_3)$ as the forcing function and ignore the $[H_3(\omega_a, \omega_b, \omega_c) \circ \delta n_s^3]\delta n_s$ term since it contributes fourth-order terms and small second-order terms. Also ignore the small contribution to the first-order terms due to $[H_2(\omega_a, \omega_b) \circ \delta n_s^2]\delta n_s$. Equate terms of the same order to get three equations:

$$j\omega_a H_1(\omega_a) \circ \delta n_s = c_n(1 - f_0) \circ \delta n_s - \frac{c_n n_{s0}}{f_0}\,H_1(\omega_a) \circ \delta n_s \tag{68}$$

$$\begin{aligned} j(\omega_a + \omega_b)H_2(\omega_a, \omega_b) \circ \delta n_s^2 = -\frac{c_n n_{s0}}{f_0}\,H_2(\omega_a, \omega_b) \circ \delta n_s^2 \\ - c_n[H_1(\omega_a) \circ \delta n_s]\delta n_s \end{aligned} \tag{69}$$

$$\begin{aligned} j(\omega_a + \omega_b + \omega_c)H_3(\omega_a, \omega_b, \omega_c) \circ \delta n_s^3 = -\frac{c_n n_{s0}}{f_0}\,H_3(\omega_a, \omega_b, \omega_c) \circ \delta n_s^3 \\ - c_n[H_2(\omega_a, \omega_b) \circ \delta n_s^2]\delta n_s. \end{aligned} \tag{70}$$

Solving (68) for H_1 gives

$$H_1(\omega_a) = \frac{c_n(1 - f_0)}{j\omega_a + (c_n n_{s0}/f_0)}.$$

Solving (69) for H_2 using (77) gives

$$j(\omega_a + \omega_b)H_2(\omega_a, \omega_b) \circ \delta n_s^2 = -\frac{c_n n_{s0}}{f_0} H_2(\omega_a, \omega_b) \circ \delta n_s^2 - \frac{c_n}{2}[H_1(\omega_a) + H_1(\omega_b)] \circ \delta n_s^2.$$

So

$$H_2(\omega_a, \omega_b) = -\frac{c_n[H_1(\omega_a) + H_1(\omega_b)]}{2\left[j(\omega_a + \omega_b) + \frac{c_n n_{s0}}{f_0}\right]}.$$

Solving (70) for H_3 using (78) gives

$$j(\omega_a + \omega_b + \omega_c)H_3(\omega_a, \omega_b, \omega_c) \circ \delta n_s^3 = -\frac{c_n n_{s0}}{f_0} H_3(\omega_a, \omega_b, \omega_c) \circ \delta n_s^3 - \frac{c_n}{3}[H_2(\omega_a, \omega_b) + H_2(\omega_a, \omega_c) + H_2(\omega_b, \omega_c)] \circ \delta n_s^3.$$

So

$$H_3(\omega_a, \omega_b, \omega_c) = -\frac{c_n[H_2(\omega_a, \omega_b) + H_2(\omega_a, \omega_c) + H_2(\omega_b, \omega_c)]}{3\left[j(\omega_a + \omega_b + \omega_c) + \frac{c_n n_{s0}}{f_0}\right]}.$$

APPENDIX D

Using Volterra Series

Given a nonlinear system with an input $u(t)$ and output $y(t)$, one may describe the system using a functional series of the form[2]

$$y(t) = y_1(t) + y_2(t) + \cdots y_n(t), \tag{71}$$

where

$$y_n(t) = \int \cdots \int h_n(t - \tau_1, \cdots, t - \tau_n)u(\tau_1), \cdots, u(\tau_n)\, d\tau_a, \cdots, d\tau_n.$$

The $y_1(t)$ term is the ordinary convolution integral that is used for linear system analysis and $h_1(t)$ is the impulse response. The kernel

$h_n(t)$ is the general impulse response. If the input $u(t)$ is changed by a gain factor ϵ, then the new output is

$$\hat{y}_n(t) = \int \cdots \int h_n(t - \tau_1, \cdots, t - \tau_n)\epsilon u(\tau_1), \cdots, \epsilon u(\tau_n)\, d\tau_1, \cdots, d\tau_n = \epsilon^n y_n(t).$$

The system can be thought of as a parallel combination of first, second, third, $\cdots$ nth order subsystems.

The following theorems deal with Volterra series in the frequency domain (7) to (9) using the circle operator defined in (17).
Let

$$u = A(\omega_1)\ o\ \cos \omega_1 t + \cdots + A(\omega_3)\ o\ \cos \omega_3 t,$$

then

$$\begin{aligned} H_1(\omega_a)\ o\ u &= H_1(\omega_1)A(\omega_1)\ o\ \cos \omega_1 t + H_1(\omega_2)A(\omega_2)\ o\ \cos \omega_2 t \\ &\quad + H_1(\omega_3)A(\omega_3)\ o\ \cos \omega_3 t \\ &= H_1(\omega_a)A(\omega_a)\ o\ \cos \omega_a t \quad a = 1, 2, 3 \end{aligned} \tag{72}$$

$$\begin{aligned} &H_2(\omega_a, \omega_b)\ o\ u^2 \\ &\quad = \text{dc terms} \\ &\qquad + H_2(\omega_1, \omega_1)A^2(\omega_1) \quad [\tfrac{1}{2}]\ o\ \cos 2\omega_1 t \\ &\qquad + H_2(\omega_2, \omega_2)A^2(\omega_2) \quad [\tfrac{1}{2}]\ o\ \cos 2\omega_2 t \\ &\qquad + H_2(\omega_3, \omega_3)A^2(\omega_3) \quad [\tfrac{1}{2}]\ o\ \cos 2\omega w_3 t \\ &\qquad + H_2(\omega_1, -\omega_2)A(\omega_1)A(-\omega_2)\ o\ \cos(\omega_1 - \omega_2)t \\ &\qquad + H_2(\omega_1, \omega_2)A(\omega_1)A(\omega_2) \quad o\ \cos(\omega_1 + \omega_2)t \\ &\quad = H_2(\omega_a, \omega_b)A(\omega_a)A(\omega_b)\ [\tfrac{1}{2}]\ o\ \cos(\omega_a + \omega_b)t, \end{aligned} \tag{73}$$

where [½] is used for dc and second-order harmonics only.

$$\begin{aligned} &H_3(\omega_a, \omega_b, \omega_c)\ o\ u^3 \\ &\quad = \text{1st-order terms} \\ &\qquad + H_3(\omega_1, \omega_1, \omega_1)A^3(\omega_1) \quad [\tfrac{1}{4}]\ o\ \cos 3\omega_1 t \\ &\qquad + H_3(\omega_2, \omega_2, \omega_2)A^3(\omega_2) \quad [\tfrac{1}{4}]\ o\ \cos 3\omega_2 t \\ &\qquad + H_3(\omega_3, \omega_3, \omega_3)A^3(\omega_3) \quad [\tfrac{1}{4}]\ o\ \cos 3\omega_3 t \\ &\qquad + H_3(\omega_1, \omega_1, -\omega_2)A^2(\omega_1)A(-\omega_2) \quad [\tfrac{3}{4}]\ o\ \cos(2\omega_1 - \omega_2)t \\ &\qquad + H_3(\omega_1, \omega_1, \omega_2)A^2(\omega_1)A(\omega_2) \quad [\tfrac{3}{4}]\ o\ \cos(2\omega_1 + \omega_2)t \\ &\qquad \vdots \\ &\qquad + H_3(\omega_1, \omega_2, \omega_3)A(\omega_1)A(\omega_2)A(\omega_3) \quad [\tfrac{3}{2}]\ o\ \cos(\omega_1 + \omega_2 + \omega_3)t \\ &\qquad + H_3(\omega_1, -\omega_2, \omega_3)A(\omega_1)A(-\omega_2)A(\omega_3) \quad [\tfrac{3}{2}]\ o\ \cos(\omega_1 - \omega_2 + \omega_3)t \\ &\qquad \approx H_3(\omega_a, \omega_b, \omega_c)A(\omega_a)A(\omega_b)A(\omega_c)\ [\text{Fraction}]\ o\ \cos(\omega_a + \omega_b + \omega_c)t. \end{aligned} \tag{74}$$

This last formula is useful for all the third-order terms but not the first-order terms.

$$[H_1(\omega_a) \; o \; u]^2 = \tfrac{1}{3}[H_1(w_a)H_2(\omega_b, \omega_c) + H_1(\omega_b)H_2(\omega_a, \omega_c) + H_1(\omega_c)H_2(\omega_a, \omega_b)] \; o \; u^3$$

$$= \overline{H_1(\omega_a)H_2(\omega_b, \omega_c)} \; o \; u^3, \tag{75}$$

where the bar is used as in (25).

Differentiating Volterra series,

$$\frac{d}{dt} y_K(t) \longleftrightarrow (j\omega_1 + \cdots + j\omega_K)H_K(\omega_1, \cdots, \omega_K) \tag{76}$$

$$[H_1(\omega_a) \; o \; u] \times u = a_1 |H_1(\omega_1)| \cos(\omega_1 t + \phi_1 + \phi_{\omega 1}) + a_2 |H_1(\omega_2)| \cos(\omega_2 t + \phi_2 + \phi_{\omega 2}) + a_3 |H_1(\omega_3)| \cos(\omega_3 t + \phi_3 + \phi_{\omega 3})] \times u.$$

For harmonic terms, i.e.,

$$\omega_a = \omega_1 \quad \omega_b = \omega_1 \rightarrow 2\omega_1$$

or

$$\omega_a = \omega_1 \quad \omega_b = -\omega_a \rightarrow \text{dc}$$

$$[H_1(\omega_a) \; o \; u] \times u = \tfrac{1}{2} A(\omega_a)A(\omega_b)H_1(\omega_a) \; o \; \cos(\omega_a + \omega_b)t.$$

For sum and difference terms,

$$[H_1(\omega_a) \; o \; u] \times u = \tfrac{1}{2} A(\omega_a)A(\omega_b)[H_1(\omega_a) + H_1(\omega_b)] \; o \; \cos(\omega_a + \omega_b)t.$$

In general,

$$[H_1(\omega_a) \; o \; u] \times u = \frac{1}{2} A(\omega_a)A(\omega_b)[H_1(\omega_a) + H_1(\omega_b)]\left[\frac{\tfrac{1}{2}}{1}\right] o \cos(\omega_a + \omega_b)t$$

$$= \frac{1}{2}[H_1(\omega_a) + H_1(\omega_b)] \; o \; u^2 \tag{77}$$

$$[H_2(\omega_a, \omega_b) \; o \; u^2] \times u = \tfrac{1}{3}[H_2(\omega_a, \omega_b) + H_2(\omega_a, \omega_c) + H_2(\omega_b, \omega_c)] \; o \; u^3. \tag{78}$$

APPENDIX E

List of Symbols

B_X, B_Y	Base pushout and lateral spreading functions.
C_d	Surface depletion capacitance.

C_I	Surface inversion capacitance.
c_n	Electron capture probability.
C_{ox}	Oxide capacitance.
C_s	Surface-state capacitance.
C_T	Thermal capacitance.
d	Depletion layer width.
D_n	Complete Fourier-transformed surface-state Volterra kernel of order n.
E	Energy level.
e_n	Electron emission probability.
$f_0, f(t)$	Direct-current and time-dependent fermi distribution functions
G_n	nth order component of Fourier-transformed surface-state Volterra kernel.
g_s	Ground state degeneracy.
h_n	Time-dependent Volterra kernel of order n.
H_n	Fourier-transformed Volterra kernel of order n.
I_{BC}	Base current injected into the collector.
I_{BE}	Base current injected into the emitter.
I_{CCI}, I_{CCS}	Intrinsic and sidewall components of dominant collector current.
$i_s(t)$	Time-dependent surface-state current.
k	Boltzmann's constant.
L_D	Intrinsic Debye length.
M_3	Third-order modulation coefficient.
n_i	Intrinsic electron density.
N_s	Surface-state density.
$n_{s0}, n_s(t)$	Direct-current and time-dependent electron surface concentrations.
P_0	Output power.
q	Electronic charge.
Q_B	Actual charge in base.
Q_{BI}, Q_{BS}	Intrinsic and sidewall components of base charge.
Q_{B0}	Total majority base charge at zero bias.
Q_C	Base-collector majority charge.
Q_E	Base-emitter majority charge.
Q_g	Gate charge.
Q_I	Surface inversion charge.
Q_s	Semiconductor charge.
Q_{ss}	Surface-state charge.
Q_0	Fixed oxide charge.
$\bar{Q}$	Mean oxide charge density in C/cm^2.
R_B	Base resistance.
R_D	Surface depletion layer resistance.
R_I	Surface inversion layer resistance.

R_{nD}	Surface depletion layer resistance for electron flow.
R_{ns}	Surface-state resistance for electron flow.
R_{pB}	Resistance to hole flow in quasi-neutral region adjacent to depletion layer.
R_{pD}	Surface depletion layer resistance for hole flow.
R_{ps}	Surface-state resistance for hole flow.
R_T	Thermal resistance.
t, t_0	Time.
T	Temperature.
T_{F0}	Low-current transit time for $V_{CB} = 0$.
u_{Fn}, u_{Fp}	Fermi potentials for electrons and holes in units of the thermal voltage.
u_s	Surface potential in units of the thermal voltage.
V_{A0}	Forward Early voltage.
V_{BC}	Base-collector voltage.
V_{BE}	Base-emitter voltage.
V_{B0}	Reverse Early voltage.
V_T	Thermal voltage (kT/q).
Y_s	Surface-state admittance.
δ	Alternating current component of.
μ_n	Electron mobility.
ω	Angular frequency.
ψ_{Fn}	Electron quasi-fermi potential in electron volts.
ψ_{MS}	Metal-semiconductor work function.
ψ_s	Surface potential in volts.

REFERENCES

1. S. T. Brewer et al., "SG Undersea Cable System: Requirements and Performance," B.S.T.J., *57*, No. 7 (September 1978), pp. 2319–2354.
2. H. E. Abraham and R. G. Meyer, "Transistor Design for Low Distortion at High Frequencies," IEEE Trans. on Electron Devices, *ED-23,* No. 12 (December 1976), pp. 1290–1297.
3. A. S. Grove and D. J. Fitzgerald, "Surface Effects on p-n Junctions: Characteristics of Surface Space-Charge Regions Under Non-Equilibrium Conditions," Solid-State Electronics, *9* (August 1966), pp. 783–806.
4. K. Lehovec and A. Slobodskoy, "Impedance of Semiconductor-Insulator-Metal Capacitors," Solid-State Electronics, *7* (January 1964), pp. 59–79.
5. K. Lehovec, "Frequency Dependence of the Impedance of Distributed Surface States in MOS Structures," Appl. Phys. Lett., *8*, No. 2 (January 15, 1966), pp. 48–50.
6. E. H. Nicollian and A. Goetzberger, "The Si-SiO_2 Interface—Electrical Properties as Determined by the Metal-Insulator-Silicon Conductance Technique," B.S.T.J., *46,* No. 6 (July–August 1967), pp. 1055–1133.
7. S. Narayanan, "Transistor Distortion Analysis Using Volterra Series Representation," B.S.T.J., *46,* No. 5 (May–June 1967), pp. 991–1024.
8. M. H. White and J. R. Cricchi, "Characterization of Thin Oxide NMOS Memory Transistors," IEEE Trans. on Electron Devices, *ED-19,* No. 12 (December 1972), pp. 1280–1288.
9. U. Kämpf and H. G. Wagemann, "Radiation Damage of Thermally Oxidized MOS Capacitors," IEEE Trans. Electron Devices, *ED-23,* No. 1 (January 1976), pp. 5–10.
10. Members of Technical Staff, Bell Laboratories, Inc., *Transmission Systems for Communication,* Winston-Salem: Western Electric, 1971, p. 247.

11. J. E. Dennis, D. M. Gay, and R. E. Welsch, "An Adaptive Nonlinear Least-Squares Algorithm," NBER Working Paper No. 196 (1977).
12. L. I. Popova, P. K. Vitanov and B. Z. Antov, "Interface States in MNOS Systems," Thin Solid Films, *51*, No. 3 (June 15, 1978), pp. 305–309.
13. F. M. Nazar, "Low-Frequency Conductance of Thermally Grown SiO_2 Films," Int. J. of Electronics, *44*, No. 6 (June 1978), pp. 657–662.
14. H. J. J. De Man, "A Fast Algorithm for the Calculation of Junction Capacitance and Its Application for Impurity Profile Determination," Solid-State Electronics, *15* (February 1972), pp. 177–187.
15. H. K. Gummel and H. C. Poon, "An Integral Charge Control Model of Bipolar Transistors," B.S.T.J., *49*, No. 5 (May–June 1970), pp. 327–852.
16. L. W. Nagel and D. O. Pederson, "SPICE (Simulation Program with Integrated Circuit Emphasis)," Electronics Research Laboratory, University of California, Berkeley, Memorandum No. ERL-M382, 1973.
17. D. G. Duff, "Modeling High Current Effects in Bipolar Transistors for Use in Computer-Aided Distortion Analysis," D. Eng. Thesis, University of California, Berkeley, 1976.
18. D. G. Duff and R. G. Meyer, "An Extended Integral Charge Control Transistor Model for High Current DC, AC and Distortion Analysis," Proc. 1977 IEEE Internat. Symp. Circuits and Systems, pp. 19–22.
19. R. J. Whittier and D. A. Tremere, "Current Gain and Cutoff Frequency Falloff at High Currents," IEEE Trans. on Electron Devices, *ED-16*, No. 1 (January 1969), pp. 39–57.
20. A. Van der Ziel and D. Agouridis, "The Cutoff Frequency Falloff in UHF Transistors at High Currents," Proc. IEEE, *54*, No. 3 (March 1966), pp. 411–412.
21. J. Choma, "A Curve-Fitted Circuits Models for Bipolar Transistor f_T Roll-Off at High Injection Levels," IEEE J. Solid-State Circuits, *SC-11*, No. 2 (April 1976), pp. 346–348.
22. P. Gray, D. DeWitt, A. Boothryd, and J. Gibbons, *Physical Electronics and Circuit Models of Transistors*, New York: John Wiley, 1964, p. 141.
23. W. M. Fox et al., "SG Undersea Cable System: Semiconductor Devices and Passive Components," B.S.T.J., *57*, No. 7 (September 1978), pp. 2405–2434.
24. H. C. Poon, "Implication of Transistor Frequency Dependence on Intermodulation Distortion," IEEE Trans. on Electron Devices, *ED-21*, No. 1 (January 1974), pp. 110–112.